2005

Noise and error propagation in diffusion tensor imaging

Shital Bipin Desai
West Virginia University

Noise and Error Propagation in Diffusion Tensor Imaging

Shital Bipin Desai

Thesis submitted to the
College of Engineering and Mineral Resources
at West Virginia University
in partial fulfillment of the requirements
for the degree of

Master of Science
in
Electrical Engineering

Dr. Donald Adjeroh, Ph.D., Chair
Dr. Aina Puce, Ph.D.
Dr. Susan Lemieux, Ph.D.
Dr. Xin Li, Ph.D.
Dr. Mark Jerabek, Ph.D.

Lane Department of Computer Science and Electrical Engineering
and Center of Advanced Imaging/Department of Radiology

Morgantown, West Virginia
2005

Keywords:

Magnetic Resonance Imaging, Diffusion Tensor Imaging, DTI, Diffusion Weighted Images, DTI invariant parameters, Fractional Anisotropy, error propagation, intervoxel coherence

ABSTRACT

Noise and Error Propagation in Diffusion Tensor Imaging

Shital Bipin Desai

Diffusion Tensor Imaging (DTI) is a unique non-invasive technique for *in vivo* visualization and analysis of white matter fiber tracts by measuring the anisotropy of water molecule diffusion in the brain tissue. DTI has been used to highlight white matter to demonstrate subtle abnormalities in neurological disorders such as stroke, dyslexia, multiple sclerosis etc. and is currently being used increasingly in clinical imaging protocols. Diffusion weighted images are affected by several artifacts and noise from the human subject and the MRI scanner. This thesis studies the error propagation in the calculation of the DTI invariant anisotropy. The main focus is on the computation of Fractional Anisotropy (FA) across an image volume using four different methods and quantitatively comparing them in terms of error propagation, filtering and computational efficiency in data sets containing either simulated or human brain data. Simulated data is an important contribution in this thesis as they serve as a platform to validate the FA results for human brain MRI data. The four methods that were used were Diffusion Tensor, Diffusion Ellipsoid, Hasan and Platonic Variance. The results showed similar trends across the simulated and real data sets for all methods. Of the four methods used to calculate FA, the Hasan method without diffusion tensor yielded best efficiency, in terms of computation time, but exhibited poor noise robustness, whereas the Platonic Variance method was more robust to noise and also provided relatively good efficiency for computation time.

DEDICATION

I am honored to dedicate this work to my parents, Kumud and Bipin Desai for their support, effort, sacrifice and encouragement during my career without which I would not be able to come this far. I express my love and gratefulness to my two sisters Neha and Sehal and my brother-in-law Jignesh for their affection, inspiration and guidance throughout my life. I thank all of them to help me follow my dreams and pursue my goals.

ACKNOWLEDGEMENTS

A few lines of acknowledgement will not be sufficient enough to express my gratefulness to all those who supported me in the last two and a half years of my Masters.

I express my sincere thanks and appreciation to Dr. Donald Adjeroh for giving me an opportunity to work with him, and for being the chair of my thesis committee. His constant support, encouragement and guidance have been a driving force to help me mature as a student and as a researcher. His dedication to help me succeed is deeply appreciated. I am greatly indebted to him for making my masters experience a memorable one. In three simple words I can say Dr. Adjeroh has been my friend, philosopher and guide in the course of this study at West Virginia University.

I am grateful to Dr. Aina Puce and Dr. Susan Lemieux, without whom this research would not have begun. Their confidence in my abilities has been unwavering which has helped to make this thesis a success. Their expert guidance and ideas have motivated me to give my best output.

Without the dedication, commitment, time and effort of my research committee, this endeavor would not have been possible.

Dr. Xin Li and Dr. Mark Jerabek, the other members of my thesis committee have been generous and patient. I thank them for their support and contribution and for serving on my committee. A special note of thanks to all of the faculty and the staff members at WVU for their excellent work and support.

I thank all my family members, relatives and friends for their well wishes and continuing support both from India as well as from the United States.

TABLE OF CONTENTS

LIST OF FIGURES

LIST OF TABLES

Chapter 1: Introduction

1.1 Motivation and the Problem

Diffusion Tensor Imaging (DTI) is an *in vivo* visualization Magnetic Resonance Imaging (MRI) technique that provides quantitative information about the integrity and orientation of the white matter tracts in the human brain. These white matter tracts carry information between the brain regions. In case of neurological disorders, DTI is an effective imaging technique that could potentially assess tract disruption. Several artifacts are introduced during the acquisition of diffusion tensor images. These artifacts are produced by certain interactions of the patient's body or body functions with the imaging process. Also the raw data from the MRI scanner will be degraded by various amounts of noise which is in the form of spurious RF energy picked up from the patient's body. In order to obtain accurate computations of the DTI indices, it is important to use robust methods to remove noise from the images while preserving tissue and anatomical details that can be found to obtain good fiber tracking results.

Image noise introduces errors in the calculated diffusion tensor and hence the calculated eigen values (principal diffusivities) and eigen vectors (principal axes). Random variations in these quantities complicate the analysis and interpretation of DTI experiments. These artifacts and noise propagate in the form of a chain of errors from the diffusion tensor (DT) to the various invariant measures of DTI. A few of these scalar invariant indices are Fractional Anisotropy (FA), Relative Anisotropy (RA) and Volume Ratio (VR). These scalar indices are widely used in clinical applications such as the study of brain development, surgical planning for brain tumor resection and characterization of white matter diseases [6].

This thesis deals with the problem of noise and error propagation in DTI. We have implemented four previously studied methods to compute the FA maps. We have suggested methods to denoise the FA maps and extended the formulae to compute the

error propagation in the various invariant anisotropies of DTI. A comparison between the four methods is made using simulated and real human brain data for estimate of accuracy as well as speed of computation.

1.2 Thesis Objective

The main objectives of this thesis are summarized as follows:

(a) To implement the proposed four methods generating FA maps. These methods include using the Diffusion Tensor calculation (Pierpaoli & Basser 1996) [2], [7], the Ellipsoid Method (Ulug & Van Zijl in 1999) [3], Hasan method (Hasan & Narayanan 2003) [4], and Platonic Variance method (Akkerman 2003) [5];
(b) To generate directional FA maps from the four methods using color coding;
(c) To denoise the FA maps and provide methods to improve their visual appearance;
(d) To test the methods of FA map calculations on simulated data and on human brain MRI data;
(e) To compute error propagation in the invariant measures of DTI;
(f) To compare results between simulated and human brain MRI data.

1.3 Thesis Contribution

In this thesis, we have:

(a) Studied the variance measure of error propagation in invariant measures such as FA and RA. We have extended this work and proposed corresponding error propagation formulae for other measures such as Volume Ratio (VR), trace, Anisotropy index (AI), and Ultimate Anisotropy (UA).
(b) Generated simulated data and obtained their FA maps using the four methods to validate the results obtained from real human brain MRI data.
(c) Implemented methods to denoise the FA maps and suggested new methods such as intervoxel coherence methods to improve the visual appearance of these maps.

(d) Provided a detailed comparison of the robustness and time efficiency of the different FA methods on simulated and human data.

1.4 Thesis Organization

This thesis is organized in six chapters. An introduction and overview of MRI, DTI its sources of error and clinical applications are briefly discussed in Chapter 2. Objectives (a) and (b) are covered in Chapter 3 which discusses various methods for computing the FA maps. Propagation of error in various DTI parameters is described in Chapter 4, and new relations are derived and proposed in Chapter 4. This chapter also deals with methods to filter the FA maps and to improve them using Intervoxel Coherence methods. Chapter 5 puts forth the results using simulated data and human brain MRI data. It also provides a comparative study on the robustness and computational efficiency of the four FA methods using simulated and human brain data. Chapter 6 concludes the thesis, examining how each of the objectives have been met, and provides some ideas for future work. The Appendix contains Figures of the brain slices taken in six different directions and FA maps for the human brain data with varying number of averages.

Chapter 2: Background

2.1 Introduction

Diffusion Tensor Magnetic Resonance Imaging (DTI) refers to the Magnetic Resonance Imaging (MRI) measurement of the direction of water diffusion within each voxel of an imaging volume and its analytical display. The use of DTI is evolving for imaging the internal structure of the brain and may help diagnose conditions that affect the white matter in the brain. MRI is a tomographic imaging technique that produces images of internal physical and chemical characteristics of an object from externally measured nuclear magnetic resonance signals, in the radio frequency range. In case of neurological disorders, DTI is an effective imaging technique that could potentially assess possible tract disruption. Diffusion is an intrinsic process that is independent of the MRI effect or the magnetic field. In theory, the diffusion along any direction in space can be measured by MRI. MRI provides access to both superficial and deep organs with high resolution without any interference with the diffusion process.

Using MRI we can distinguish between the gray matter, white matter and cerebrospinal fluid of the human brain. Gray matter contains the brain cells or neurons, is relatively dark in color and consists of masses of cell bodies and dendrites. White matter is the heavily myelinated central nervous tissue, light in color and consisting of bundles of axons. In general, gray matter represents information processing centers in the brain, and white matter represents the networking of – or connections between – these processing centers [36]. Cerebrospinal fluid is a clear watery liquid that surrounds and protects the brain from mechanical injury by acting as a shock absorber [37]. It is also a transport medium for important brain nutrients and chemical messengers. The white matter appears homogeneous in the structural MRI images and we are unable to observe the white matter tracts directly. However, with DTI, the imaging is sensitive to the anisotropic diffusion within the white matter tracts of the brain. Potential applications in neurology and neurosurgery include disturbances of white matter tracts caused by neurosurgery, the presence of brain tumors and associated edema (swelling), ischemia

(brain damage from restricted blood flow) and certain types of brain tumors. In the rest of this chapter, a general background on the principles of MRI, principles of DTI and sources of error for DTI have been briefly discussed.

Diffusion weighted MRI methods such as DTI techniques, provide images that are sensitive to the random displacement of water molecules. These molecules move freely in a glass of water whereas their motion is restricted in highly compartmentalized structures such as brain tissue. Thus the water molecules in most brain regions will have a lower diffusion coefficient compared to those in a glass of water. This diffusion coefficient reflects the amount of net diffusion the water molecules experience. We can use MRI to calculate pictures and maps of diffusion coefficients, called apparent diffusion coefficient (ADC), of the brain.

2.2 Magnetic Resonance Imaging (MRI)

2.2.1 Origins and Development of MRI

The first successful Nuclear Magnetic Resonance (NMR) experiment was performed in 1946 by ***Felix Bloch*** and ***Edward Purcell***. In the years 1950-1970 NMR was developed and used for physical and chemical molecular analysis of solid inanimate and inert molecules. In 1971, ***Raymond Damadian*** showed that the nuclear magnetic relaxation times of tissues and tumors differed, thus motivating scientists to consider magnetic resonance for the detection of disease. In 1973, MRI was first demonstrated on small test tube samples by ***Paul Lauterbur*** working in the USA and independent to ***Sir Peter Mansfield*** working in the United Kingdom***.*** Lauterbar and Mansfield received the Nobel Prize for Physics in 2004 for their respective contributions for producing magnetic resonance images in two dimensions for the first time [39]. In 1975, ***Richard Ernst*** proposed magnetic resonance imaging using phase and frequency encoding, and image reconstruction using the Fourier Transform. This technique is the basis of current MRI techniques. In 1977, ***Raymond Damadian*** demonstrated MRI of the whole body [30]. MRI continues to be a growing science.

2.2.2 Principles of MRI

Routine clinical NMR imaging involves acquiring the resonant signal from the proton in the hydrogen nuclei found abundantly in the human body in the form of water molecules. Originally called “nuclear magnetic resonance imaging” the confusion caused by the word associated with radioactive phenomena led to the use of the simpler term “magnetic resonance imaging”. The term “imaging” comes from the fact that these data are acquired in two dimensions.

There are various references that review an overview of MRI principles [1], [33], [12], [26]. The introduction material below primarily follows the description in [1]. The basic principles of MRI can be given as:

1. the protons in the body are excited using radio frequency (RF) energy;
2. after a delay the protons emit the RF energy;
3. the resulting emitted RF energy from the tissue is sampled using a specialized receiver;
4. the sampled data are reconstructed to form a two dimensional image of the particular region of interest in the body being studied.

The wavelengths used in MRI are the RF range. The signals from the excited protons can be detected. The MRI image is made up of a set of signals which depend on three main parameters: proton density, ρ and relaxation times, T_1 and T_2

Proton density describes the number of protons in one unit volume. Protons can be considered as tiny bar magnets with north and south poles. In the absence of a magnetic field the protons are randomly oriented. However, when subjected to a magnetic field B_0 , they orient themselves in the direction of the magnetic field and reach an equilibrium magnetization. Transmission of energy to the protons excites and forces the net magnetization to flip transiently from their equilibrium position. When the excitation is interrupted, the magnetization returns back to equilibrium position, i.e. relaxes. During relaxation, the protons emit MRI signals that are collected to generate a two dimensional MRI image [35].

The relaxation time can be split up into two components:

T_1: Spin-lattice relaxation time,

T_2: Spin-spin relaxation time.

The magnetization vector, **M**, represents the resultant of the protons, whose orientation depends on the proportion of protons in the parallel or antiparallel position. T_1 characterizes the return of the **M** vector to equilibrium along the longitudinal axis defined by B_0. T_1 results from the interaction between the protons and the whole environment. T_1 characterizes the efficiency of the environment in absorbing the energy of excited protons during relaxation: T_1 is short when the environment has a high efficiency for absorbing energy (*i.e.* absorbs the energy faster) as in the case of fat; it is long in the opposite case, as in pure water.

T_2 characterizes the dephasing individual protons with respect to each other causing a decrease in the magnitude of the **M** vector in the transverse plane perpendicular to B_0. T_2 is called the spin-spin relaxation time because it is the result of interactions between neighboring protons. Since each proton is a tiny magnet, it creates a micromagnetic field, disturbing the neighboring protons, leading to a loss of phase coherence. The tissues in which there are relatively significant microvariations added to B_0 rapidly lose phase coherence i.e. T_2 is short as in the case of fat. When the microvariations have relatively little effect in other tissues; T_2 is long as in the case of pure water [14].

Thus the relaxation times depend on the biological state of tissues and in just the same way that different people vary in weight and height, tissues have different T_1 and T_2. T_1 and T_2 remain constant in a given tissue in a given state. The range of T_1 and T_2 in the human body is: T_1: 300-2000 ms; T_2: 30-150 ms, for the standard range of field strengths. The intensity at each point of an MR image is a blend of the proton density ρ, T_1 and T_2. It is also possible to monitor the proportional effects of ρ, T_1 and T_2 [1].

Protons are excited by energy supplied in the form of low energy electromagnetic waves or RF. This energy is not transmitted by the transmitter coil continuously, but in short pulses. A pulse sequence is a succession of RF pulses (90^0 pulse i.e. **M** rotates to an angle of 90^0 to its equilibrium position, 180^0 pulse i.e. inversion of **M** with respect to B_0) at varying time intervals. The time intervals are:

Repetition time (TR): This is the time interval between the beginnings of two consecutive data acquisition and is chosen by the operator.

Echo time (TE): Time between the beginning of the sequence and the middle of the echo.

The pulse sequence used for diffusion imaging is based on the spin echo.

Spin Echo (SE):

This is a most frequently used pulse sequence. Each pulse consists of two RF pulses: 90^0 and then 180^0. The 90^0 pulse produces a signal which cannot be used to generate an image; 180^0 pulse generates a signal which can be used to produce an image. The 180^0 RF pulse reflects the first signal in the form of an echo signal that increases then decreases. Spin echo is widely used as it is considers all the three parameters proton density, T_1 and T_2 for diagnosis. It generates T_1 and T_2 weighted images.

2.2.3 The MRI Scanner

A mobile bed, or gurney, facilitates insertion of the patient into the machine. The area of the tissue to be studied is positioned at the center of the magnet. The key elements of a MRI system include:

1. Super conducting cryogen-cooled electromagnet
2. RF emission/reception coil
3. Gradient coils
4. Data collection and processing systems
5. Power supplies

6. Control and display console

Figure 2.1: The MRI scanner [2]

The MRI scanner uses magnetic and RF fields to create cross sectional images or slices of the human body. The main component of the MRI scanner is a large tube shaped or cylindrical magnet with strength between 0.1 Tesla and 7.0 Tesla. The MRI scanner in the Center for Advanced Imaging at WVU is 3.0 Tesla and has a bore width of 55cm.

To begin a clinical MRI examination, the patient lies on a mobile table and is then moved inside the MRI scanner's bore where the magnetic field is created. Each clinical MRI examination typically is comprised of a series of 6 to 15 sequences, with each sequence lasting between 0.5 and 5 minutes. An "MRI sequence" is an acquisition of data that yields a specific image orientation and a specific type of image appearance or "contrast." Thus a typical exam can last for a total of ten minutes to an hour, depending on the type of exam being run and the MRI scanner being used [1].

During the examination, the RF pulses are repeated and subsequently the energy which is absorbed by different atoms in the body is echoed or emitted back out of the body. These echoes are continuously measured by the MRI scanner and a digital computer reconstructs these echoes into images of the body. The clanging and banging heard during the MRI exam is created when gradient coils are rapidly switched on and off to spatially localize the MRI signal being emitted from the patient's body. An important benefit of MRI is that it can easily acquire direct views of the body in any orientation, while CT scanners only acquire images perpendicular to the long body axis [2].

A few important parameters associated with the MRI system include:

Field of View (FOV): It is defined as the size of a two dimensional spatially sampled area which makes the image. It is the square image area that contains the object of interest to be measured. The smaller the FOV, the higher the resolution and the smaller the voxel size but the lower the measured signal. The right choice of FOV is important for MR image quality and depends on the body part being imaged [33]. It ranges from 10 to 50 cm for most machines.

Slice Thickness: It is the thickness of an imaging slice. For optimal image quality it is important to choose the best fitting slice thickness for an examination. When a small item of interest is contained within the slice thickness with other tissue of differing signal intensity then the resulting signal displayed on the image is a combination of these two intensities. If the slice is the same thickness or thinner than the small structure of interest, only that structures signal intensity is displayed on the image [33]. It ranges mainly from 3 to 15 mm.

Matrix Size: All digital techniques consider images to be divided into a matrix of pixels – or two dimensional individual image components. For each pixel, the MR signal intensity is represented on an 8-bit gray scale. The pixels together form a two dimensional image matrix. By contrast, voxels are three dimensional entities that are sampled in the two dimensionality image space. Three dimensional voxels are represented by two dimensional voxels making up the MR image with the third dimension being filled out by multiple slices. The most commonly used matrix size is 256×256.

Number of Excitations: Every individual signal needed to generate an MRI image can be acquired once or several times with repeated excitations generating an average image. With more excitations the average error in the measurements decreases resulting in more precise measurements. However, this lengthens image acquisition time which can then result in imaging artifacts when the subject moves. The number of excitations typically ranges from 1 to 6.

2.2.4 MRI Views of Human Brain

The brain can be sliced or sectioned in three orthogonal planes: axial, coronal and sagittal as shown in the Figure 2.2.

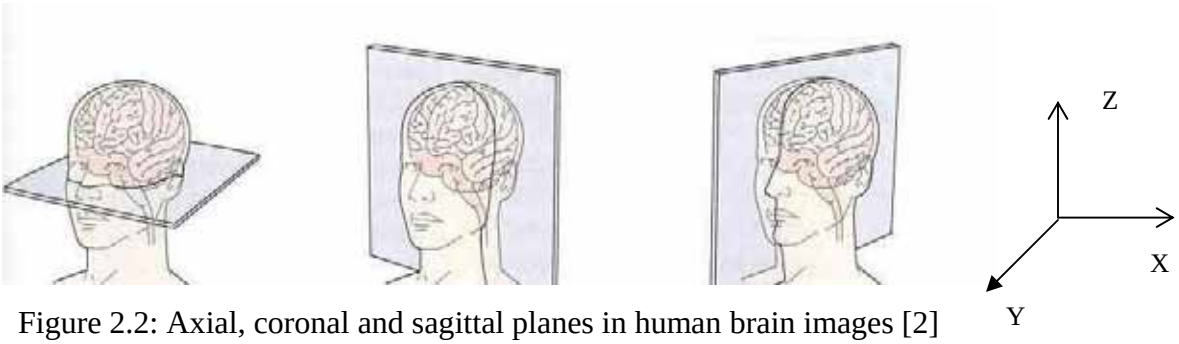

Figure 2.2: Axial, coronal and sagittal planes in human brain images [2]

Axial/Transverse $(X-Y)$**:** Axial sections form a series of circumferential slicing- like slicing the human brain into series of pancakes and stacking them one over the other.

Coronal $(X-Z)$**:** Coronal sections follow from front (anterior) to back (posterior). It is as though cutting through a corona, or halo, around the head.

Sagittal $(Y-Z)$**:** Sagittal sections follow from one side of the body to the other i.e. left to right or right to left. In anatomy, lateral means outside and medial means inside.

Example MRI pictures of slicing through the brain in different orientations are as shown:

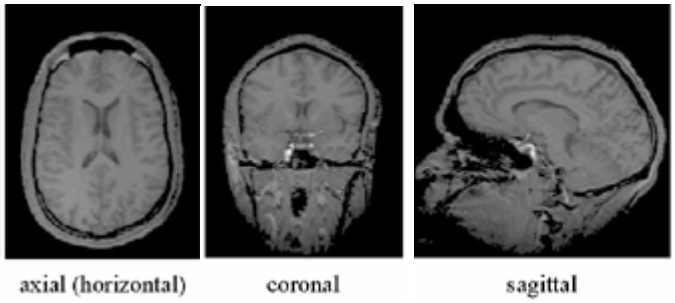

Figure 2.3: MRI slices in different orientations [3]

2.3 Diffusion Tensor Imaging (DTI)

Diffusion accounts for the net movement of a substance from an area of high concentration to an area of lower concentration in the absence of other pressures or forces. It is greater in fluids and restricted in the cellular tissue environment. Diffusion Tensor Magnetic Resonance Imaging (DT-MRI), commonly known as diffusion tensor imaging (DTI) is a non-invasive method that is used to determine the orientation and integrity of the white matter tracts *in vivo* [12]. One method to estimate these white matter tracts using DTI is called tractography. DTI is the only clinical means of non-invasively imaging the myelinated axonal structure of the human brain. However in 1986 when Le Bihan introduced the concept of diffusion imaging [2], the clinical applications faced several restrictions like motion sensitivity which caused severe ghosting artifacts and signal loss. While observing molecular displacement in micrometers, any motion, even unavoidable involuntary head motion or physiological, cardiac related pulsations of the brain tissue, can interfere with the measurement. When scans must be obtained from disoriented and confused stroke patients or young children, who can move their head excessively, scan quality can be severely compromised. All these limitations and restrictions were a major motivation for the development of faster sequences that are more robust to different motion types [14].

2.3.1 Principles of Diffusion

Diffusion refers to a process by which molecules continually intermingle as a result of their kinetic energy which transfers into random motion if they are relatively unbound as in a solution. The tendency towards increased diffusion is strong at room temperature because of the high molecular velocities associated with the thermal energy of the particles [26]. Molecular diffusion is referred to as Brownian motion. In 1827 Robert Brown observed the chaotic movement of plant spores on the water's surface and called the phenomenon water diffusion. Molecular motion is affected by the properties of the medium in which it occurs. Diffusion within a biological tissue is affected by both the tissue structure and its architecture at the microscopic level. All biological tissues exhibit

the property of movement of water molecules by Brownian motion. Instead of the water molecules moving with a fixed velocity the movement varies. For a particle undergoing Brownian motion, the Einstein relation for time and distance is given by [4]:

$$D = \frac{1}{6\tau} r^2 \tag{1.1}$$

where D is the Diffusion coefficient, τ is period of time during which a particle undergoes Brownian motion, r is the net displacement.

When the environment is restricted, the particles undergoing Brownian motion are displaced with greater magnitudes in directions parallel to the boundary and smaller magnitudes in directions perpendicular to the boundary. Thus directionally dependent Brownian motion reflects the underlying structure of the bounded environment. Diffusion is said to be anisotropic when displacement due to Brownian motion is directionally limited. Anisotropy is used to describe the different the rates and directions of diffusion in a tissue [21].

In anisotropic diffusion, the Einstein relation is generalized as:

$$D = \frac{1}{6\tau} \left\langle \hat{r}\hat{r}^t \right\rangle \tag{1.2}$$

where D is a second order tensor, $\hat{r}$ is the displacement vector indicating both magnitude and direction for Brownian motion and $\left\langle \hat{r}\hat{r}^t \right\rangle$ represents matrix dot operator. In this case D is known as the diffusion tensor [4].

Fractional anisotropy (FA) is the most commonly used scalar measure of anisotropy in DT-MRI. It represents the degree of anisotropy in the diffusion tensor. It is zero in isotropic diffusion and is equal to unity when diffusion is anisotropic. In general a higher value of FA occurs when local diffusion has a higher degree of isotropy [17], [21]. Diffusion values determined by MRI might be a composite from several structural compartments (extracellular and intracellular) within a voxel. There can be different diffusion coefficient values within these compartments. Since there is movement of fluid in and out of the blood vessels and the tissues, we cannot exactly measure the diffusion in

the tissue – it is not a closed system Therefore MRI does not give the true diffusion values, but only apparent diffusion coefficients (ADC's) [33].

The measurement of water diffusion in tissues is based on the movement of water molecules within the tissue environment. In pure liquids, such as water, individual water molecules are in constant motion in every direction due to random motion. In tissues, however, the presence of various tissue components (larger molecules, intracellular organs, membranes, cell walls, etc.), restrict the Brownian motion. In many tissues, when averaged over the macroscopic scale of image voxels, this restriction is identical in every direction, i.e., the diffusion is isotropic. In some very structured tissues, however, such as muscle or cerebral white matter, cellular arrangement shows a preferred direction of water diffusion that is largely uniform across the entire voxel, i.e., the diffusion is anisotropic. This possible selectivity in orientation is the key in using diffusion in analysis of physiological structures.

In general the diffusion tensor depends on particle mass, size, structure of the medium and temperature. In DTI, the particle mass of water molecules and the temperature at which the measurements are conducted is assumed constant. This assumption allows the DTI to be determined in terms of local anatomical structure.

2.3.2 The Imaging Process

Diffusion imaging is based on the principle that the diffusion motion of the molecules produces a dephasing of the spinning protons within a voxel that result in a reduced MR signal intensity and image brightness. The dephasing is produced by applying additional diffusion sensitizing gradients during the image acquisition cycle. Two gradients, one applied before the 180^0 RF pulse and the second applied after the pulse are used in conjunction with the pulse sequence as shown in Figure 2.4. During the time of the gradient, the spinning protons will be in different field strengths spinning at different rates along the direction of the gradient. This produces a dephasing of the protons within the voxel. When the 180^0 RF pulse is applied it reverses the spin

direction. Now, when the second gradient is applied, it produces a rephasing on the spinning protons within the voxel [35].

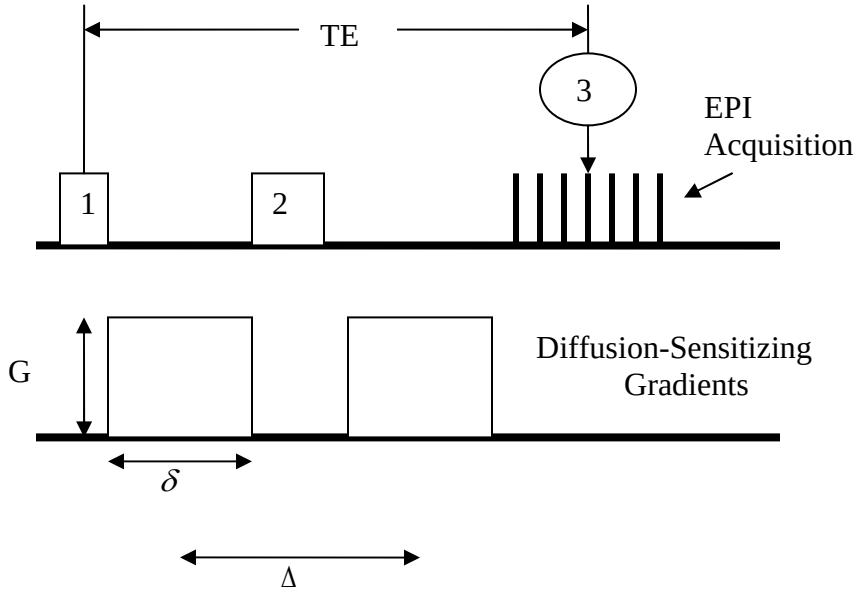

1: 90^0 RF Pulse
2: 180^0 RF Pulse
3: Echo Event

G: Pulse gradient strength
δ: Pulse duration
Δ : Pulse separation

$$b = \gamma^2 G^2 \delta^2 \left(\Delta - \delta/3\right)$$

Figure 2.4: Diffusion acquisition [35]

However, only the protons that have not moved or changed positions between the times of the two gradients will be completely rephrased. The protons in molecules that have moved will be in a different location and field strength during the second gradient and will not be completely rephrased. This results in reduced signal intensity that produces the contrast of the diffusing molecules with respect to the non-moving tissue structure [35].

2.3.3 Neural Structure and Diffusion Tensor Imaging (DTI)

Our brain is made up of approximately 100-billion nerve cells called neurons. Neurons are cells in the nervous system that transmit electrochemical signals in the form of nerve impulses over long distances, from one part of the body to another. They are composed of three basic parts: cell body or soma, the axon and dendrites or endings. Dendrites are tree-like branches attached to the neuron cell body and receive impulses from other neurons at synapses [4]. Axons are long cable-like structures that transmit information away from the cell body and dendrites as shown in Figure 2.5. Axons are wrapped by a thin layer of connective tissue known as endoneurium. Groups of wrapped axons are bundled together in tracts or fascicles, by a thin boundary known as perineurium.

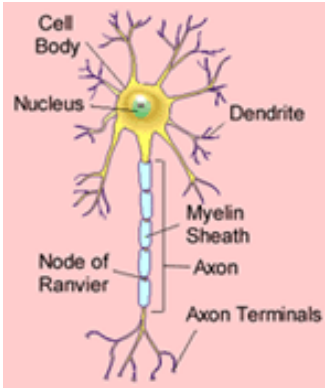

Figure 2.5: Structure of a myelinated neuron [32]

The portion in the human brain that contains white fatty myelinated Schwann cells forms the white matter in the brain. The ability of water to diffuse across tracts with myelinated boundaries is restricted, causing water to diffuse anisotropically in greater amounts in directions parallel to fiber tracts and in lesser amounts of diffusion in directions towards the boundaries. This physical situation of increased water diffusion in directions parallel to myelinated fascicles is what is measured in diffusion weighted images to construct diffusion tensors which are 3x3 symmetric matrices that capture directional variation in the diffusion rates and resulting tractography estimates that compute the pathways of the complete nerve fiber tracts. In DTI maps, white matter

tracts, which exhibit a high anisotropy index, appear bright. Gray matter and cerebrospinal fluid, on the other hand, are represented by dark shades according to their low or absent anisotropy. Several acquisitions of image data with diffusion weighting along different directions are taken. A minimum case needs seven diffusion weighted images out of which six images are acquired with gradients in at least six non collinear directions and one is an unweighted T2 image. The six images on combining using the Stejskal-Tanner equation (as explained in Chapter 3) generates a system of six linear equations with six unknowns which in turn are solved to yield the apparent diffusion coefficients [4].

2.4 Sources of Error in DTI/MRI

The main artifacts in DTI data are those associated with acquiring the diffusion weighted images from which the diffusion tensor is estimated. Artifacts are undesirable objects, such as streaks and spots that appear in images which do not directly represent an anatomical structure. They are produced by certain interactions of the patient's body or body functions with the imaging process. In a DTI examination, images with different directions of diffusion weighting are recorded from multiple slices of the subject's brain. Eddy currents and geometric distortions between images with different diffusion sensitizing directions, may cause deformed depictions of the brain slices. To correct this, the distortion effect must be modeled and elastic alignment algorithms are applied such that the geometric deformation is reversed [16]. Other artifacts can include subject motion and magnetic susceptibility effects. Patient motion is the largest artifact, often resulting from head and body movements (e.g. eye movements and swallowing) and other physiological artifacts (e.g. respiration, cardiac motion). Movement of the imaged object during the sequence results in inconsistencies in phase and amplitude which leads to blurring and ghosting effects [20].

Magnetic susceptibility is the extent to which a material becomes magnetized when placed within a magnetic field. Magnetic susceptibility artifacts occur as a result of microscopic gradients or variations in the magnetic field strength that occurs near the interfaces of substances of different magnetic susceptibility. It may

occur due to a medical device or an object near or in an imaging field of view whose magnetic susceptibility is different from the tissue [33].

The raw data from the MRI scanner will be degraded by various amounts of noise which is in the form of random, unwanted RF energy. Some noise might be generated within the receiver coil or other electronics, but it is usually much less than the noise from the patient's body [37]. In order to obtain accurate computations, it is important to use robust methods to remove noise from the images while preserving edges and anatomical details that can be found to obtain good fiber tracking results. Hardware issues such as background gradients, gradient non-linearity and miscalibration also cause error in the measurement [22].

Another artifact called the partial voluming is caused by the size of the image voxel. For example, if a small voxel contains only fat or water signal, and a larger voxel might contain a combination of the two, the large voxel possesses signal intensity equal to the weighted average of the quantity of water and fat present in the voxel. Another manifestation of this type of artifact is a loss of resolution caused by multiple features present in the image voxel [34]. This is important in DTI, as this will occur in regions where tracts traveling in different directions come together.

2.5 Clinical Uses of DTI Techniques

DTI has great potential as a tool for neurological research and clinical applications [16]. Loss of tissue structure, due to a brain injury, can result in an increase in the ADC's and cause a reduction in FA. DTI allows us to image these processes and to potentially determine how they are related to disability and cognitive impairment. DTI provides quantitative information which can be used to compare numbers between different patients, or between the same patient imaged at different times. This allows us to monitor the structural changes in the white matter taking place in the brain over a period of time. Water proton diffusion anisotropy abnormalities have been reported in a variety of disorders: stroke, schizophrenia, alcoholism, developmental dyslexia, multiple sclerosis and in the normal brain development in the new born [16]. Based on geometry

and the degree of anisotropy loss, white matter tract pathology such as dislocation, infiltration, swelling and disruption can be documented [38]. Disruption in the brain connectivity resulting from physical trauma, brain tumor, infection with human immunodeficiency virus can be quantified using DTI. Diffusion MRI provides some patients with the opportunity to receive suitable treatment at a stage when the brain tissue might still be salvageable [23]. For example: a neurosurgical procedure which can avoid damaging these crucial structures in the brain as the neurosurgeon can plan his or her surgical approach based on this imaging data.

Chapter 3: Computing Fractional Anisotropy Maps

3.1 Diffusion Tensor and Diffusion Weighted Imaging

Fractional Anisotropy (FA) is the most commonly used DTI invariant index. It is a measure of the fraction of magnitude of the tensor that can be ascribed to the anisotropic diffusion. It ranges from 0 to 1 i.e. from isotropic diffusion to diffusion along a single direction. Diffusion weighted MRI uses diffusion gradient pulses to weight the signal by the relative amount of diffusion in the measurement direction, $\hat{g}$ [7]. Diffusion weighted images are used as the raw data source that for the input for the diffusion tensor calculation. To measure the diffusion tensor, diffusion-weighted acquisitions in at least six different directions must be performed, yielding an equal number of apparent diffusion coefficients (ADCs). Taking more than six diffusion weighted measurements creates an over constrained system of equations which may be solved using the least squares approach [40].

Diffusion values determined by MRI might be a composite from several structural compartments (extracellular and intracellular) within a voxel. There could be different diffusion coefficient values within these compartments. Since there is movement of fluid in and out of the blood vessels and the tissues, we cannot exactly measure the diffusion in the tissue – it is not a closed system. Therefore MRI does not give the true diffusion values, but only the ADCs. The ADC for a given direction is calculated on a pixel-by-pixel basis by fitting signal intensities to the Stejskal-Tanner equation [9], [7] as shown below:

$$S(n) = S(0)\exp(-bADC) \tag{3.1}$$

where

$$b = \gamma^2 G^2 \delta^2 \left(\Delta - \delta/3\right) \tag{3.2}$$

$S(n)$ is the intensity of the image in the n^{th} direction and $S(0)$ is the intensity of the unweighted image. ADC can be computed using the following equation:

$$ADC = \frac{\ln S(0) - \ln S(n)}{b} \tag{3.3}$$

However, these ADC maps are not the diffusion tensor elements. Let ADC_{ijk} denote the diffusion map obtained from data along the direction $\left(G_x, G_y, G_z = (i, j, k)\right)$. For example, ADC_{110} is the ADC map when G_x and G_y are applied simultaneously. The diffusion tensor elements are given by $D_{xx}, D_{yy}, D_{zz}, D_{xy}, D_{xz}, D_{yz}$ in the *x*, *y*, *z*, *xy*, *xz*, *yz* directions respectively. If only G_x is applied, then $ADC_{100} = D_{xx}$ and so on. However if more than one gradient is applied simultaneously, then the expression will involve off - diagonal elements for the diffusion tensor. For example, the relation between ADC_{110} and the elements of the tensor is given by:

$$ADC_{110} = D_{xx} + D_{yy} + 2D_{xy} \tag{3.4}$$

If we define gradients as:

$$\left(G_x, G_y, G_z\right) = \left\{(1,1,0),(1,0,1),(0,1,1),(-1,1,0),(-1,0,1),(0,-1,1)\right\} \tag{3.5}$$

then we can express the ADC in terms of the tensor elements:

$$\begin{aligned}
ADC_{110} &= D_{xx} + D_{yy} + 2D_{xy} \\
ADC_{101} &= D_{xx} + D_{zz} + 2D_{xz} \\
ADC_{011} &= D_{yy} + D_{zz} + 2D_{yz} \\
ADC_{-110} &= D_{xx} + D_{yy} - 2D_{xy} \\
ADC_{-101} &= D_{xx} + D_{zz} - 2D_{xz} \\
ADC_{0-11} &= D_{yy} + D_{zz} - 2D_{yz}
\end{aligned} \tag{3.6}$$

In matrix form it can be expressed as:

$$\begin{bmatrix} ADC_{110} \\ ADC_{101} \\ ADC_{011} \\ ADC_{-110} \\ ADC_{-101} \\ ADC_{0-11} \end{bmatrix} = \begin{bmatrix} 1 & 1 & 0 & 2 & 0 & 0 \\ 1 & 0 & 1 & 0 & 2 & 0 \\ 0 & 1 & 1 & 0 & 0 & 2 \\ 1 & 1 & 0 & -2 & 0 & 0 \\ 1 & 0 & 1 & 0 & -2 & 0 \\ 0 & 1 & 1 & 0 & 0 & -2 \end{bmatrix} \begin{bmatrix} D_{xx} \\ D_{yy} \\ D_{zz} \\ D_{xy} \\ D_{xz} \\ D_{yz} \end{bmatrix} \tag{3.7}$$

The above matrix equation can be written as:

$$\overline{ADC} = M\overline{D} \tag{3.8}$$

where $\overline{ADC}$ is a vector of the measured elements, $\overline{D}$ is a vector of diffusion tensor elements and M is a transformation matrix that depends on the diffusion directions and relates $\overline{ADC}$ to $\overline{D}$. In the above matrix equation the diffusion tensor, $\overline{D}$ is the unknown quantity which can be determined via the inverse relation [18]:

$$\overline{D} = M^{-1}\overline{ADC} \tag{3.9}$$

For a square matrix, the inverse is straightforward. However, when we consider more than six directions i.e. for a non-square matrix, the inverse matrix is generated using the least squares approach [40]:

$$M^{-1} = \left(M^T M\right)^{-1} M^T \tag{3.10}$$

The diffusion tensor is a second rank positive 3x3 matrix:

$$D = \begin{bmatrix} D_{xx} & D_{xy} & D_{xz} \\ D_{yx} & D_{yy} & D_{yz} \\ D_{zx} & D_{zy} & D_{zz} \end{bmatrix} \tag{3.11}$$

The three diagonal diffusion coefficients D_{ii} correspond to diffusion along orthogonal *x, y* and *z* axes and there are three off-diagonal coefficients for off-axis contributions. In the interior of the brain the on diagonal elements of the tensor matrix are positive, whereas the off-diagonal elements can be positive or negative. The diffusion tensor matrix has non-negative Eigen values and thus it can be represented as an ellipsoid [17].

In physics and engineering terminology, a tensor describes directional tension forces in solid bodies using an array of three dimensional vectors. Ellipsoids are used to represent these tensors where the three major axis are the three orthogonal directions of the co-ordinate system. The directions of the main axis of the ellipsoid represent the Eigen vector and its length is the Eigen value. In DTI we compute the tensor for every voxel of the entire sampled tissue volume. In order to compute the diffusion tensor, images are obtained from at least six independent diffusion encoding directions. For each

voxel, the longest main axis of the diffusion ellipsoid represents value and direction of maximum diffusion, whereas the shortest axis denotes value and direction of minimum diffusion. If the three Eigen values are equal, then the diffusion is said to be isotropic and the diffusion tensor can be visualized as a sphere, the $FA = 0$, otherwise the diffusion is anisotropic and $FA > 0$.

Diffusion can be classified as linear or planar. When the main axis of the diffusion ellipsoid is much larger than the other two axes, it is called 'linear diffusion'. The term 'planar' indicates that diffusion is restricted along one direction only and unrestricted along the other two directions. DTI data can be analyzed in several ways and the most common way is to characterize the overall displacement of water molecules by computing the mean diffusivity in the voxel. To obtain this we compute the trace of the diffusion tensor, the mean diffusivity is given as Trace(D)/3. In order to compute the anisotropy, there are several measurements which are rotationally independent i.e. not dependent on the absolute orientation of the diffusion tensor ellipsoid. The most commonly used terms, first proposed by Basser [2], are:

(1) Relative Anisotropy (RA), a normalized standard deviation representing the ratio of the anisotropic part of the tensor to its isotropic part;

(2) Fractional Anisotropy (FA), a measure of the fraction of the magnitude of the tensor that can be ascribed to anisotropic diffusion; and,

(3) Volume Ratio (VR), a measure representing the ratio of the ellipsoid volume to the volume as a sphere of radius λ, where λ is the average of the Eigen values.

(4) Trace(D) is an anisotropic invariant computed as the sum of the diagonal elements of the diffusion tensor matrix;

(5) Radius, Surface area, and Volume of diffusion, $D_{av}, D_{surf}, D_{vol}$, respectively are used to describe the diffusion ellipsoid.

3.2 The Diffusion Tensor Method

The diffusion tensors in MRI are given by a 3x3 symmetric matrix, whose values are measured relative to the co-ordinate reference frame for the tissue in the MRI

scanner. Since they are real values, the diffusion tensor on diagonalization will generate three real Eigen values $\lambda_1, \lambda_2, \lambda_3$ and each of these has a corresponding orthogonal Eigen vector v_1, v_2, v_3 respectively [18]. The Eigen values are non-negative since negative diffusivity is physically undefined. The Eigen vectors represent the orientation of the diffusion tensor. The Eigen system of the diffusion tensor can be interpreted graphically as an ellipsoidal surface with the semi-major axis oriented in v_1 direction and the two semi minor axes in the v_2 and v_3 directions. The lengths of the axes are given by the corresponding Eigen values, i.e. λ_1 represents the length of the semi-major axis whereas λ_2 and λ_3 represent the semi-minor axes of the ellipsoid. The principal (or major) Eigen vector is the one associated with the largest Eigen value and corresponds to the direction of fastest diffusion. The Eigen values are further used in computing rotationally invariant anisotropy metrics like FA, RA, and VR [2].

$$FA = \frac{\sqrt{3\left[\left(\lambda_1 - \lambda\right)^2 + \left(\lambda_2 - \lambda\right)^2 + \left(\lambda_3 - \lambda\right)^2\right]}}{\sqrt{2\left(\lambda_1^2 + \lambda_2^2 + \lambda_3^2\right)}} \tag{3.12}$$

where:

$$\lambda = \frac{\lambda_1 + \lambda_2 + \lambda_3}{3} \tag{3.13}$$

$$RA = \frac{\sqrt{\left(\lambda_1 - \lambda\right)^2 + \left(\lambda_2 - \lambda\right)^2 + \left(\lambda_3 - \lambda\right)^2}}{\sqrt{3\lambda}} \tag{3.14}$$

$$VR = \frac{\lambda_1 \lambda_2 \lambda_3}{\lambda^3} \tag{3.15}$$

FA and RA vary between 0 (isotropic diffusion) and 1 ($\sqrt{2}$ for RA) (complete anisotropy). VR represents the ratio of the ellipsoid volume to the volume of a sphere of radius λ, its range is from 1 (isotropic diffusion) to 0.

Based on the Eigen values, diffusion can be categorized in three cases:

Linear Diffusion ($\lambda_1 >> \lambda_2 \approx \lambda_3$): In this case diffusion is mainly in the direction of the Eigen vector with the largest Eigen value.

Planar Diffusion ($\lambda_1 \approx \lambda_2 >> \lambda_3$): Diffusion is in the plane spanned by two Eigen vectors with maximum Eigen value.

Spherical Diffusion ($\lambda_1 \approx \lambda_2 \approx \lambda_3$): Diffusion is isotropic i.e. the same in all the directions

3.3 Generating Color Coded Principle Eigen Vector Weighted Maps of Fractional Anisotropy

The most common visualization goal is to highlight the spatial patterns of the principal Eigen vectors in regions which are physiologically meaningful instead of a completely specifying all of the tensor information. Visualizing these patterns is an important step in verifying that a given DTI scan has succeeded in resolving the needed feature [10]. A most simple spherical colormap of the principal Eigen vector is the standard method to generate the color FA maps [11]. FA loses directional information; hence it is essential to generate the colormaps to represent fiber tract direction.

From the given Eigen values $(\lambda_1, \lambda_2, \lambda_3)$ the one which has the maximum value and its corresponding Eigen vector i.e. the principal Eigen vector is chosen. The x, y, z components of the principal Eigen vector are compared and the color is assigned in the following manner

$$color = \begin{cases} red; & \left(|v_{1x}| > |v_{1y}| \&\& |v_{1x}| > |v_{1z}|\right) \\ green; & \left(|v_{1y}| > |v_{1x}| \&\& |v_{1y}| > |v_{1z}|\right) \\ blue; & \left(|v_{1z}| > |v_{1x}| \&\& |v_{1z}| > |v_{1y}|\right) \end{cases} \tag{3.16}$$

3.4 The Diffusion Ellipsoid Method

DTI describes the direction of diffusion in tissues in a manner which is orientation co-ordinate system dependent. An alternative approach using the diffusion ellipsoid properties was suggested by Ulug and Zigl in 1999[3]. Instead of using the Eigen values,

the diffusion is characterized by a set of three rotationally invariant quantities that have magnitude and directions of true diffusion constants and contain information about the average radius, surface and volume of diffusion ellipsoid [3]. These scaled invariant quantities generate a new set of orientation independent anisotropies [which are also normalized between 0 (isotropic) and 1 (completely anisotropic)] but that do not involve tensor diagonalization and Eigen value determination. This can reduce the susceptibility to potential artifacts caused by numerical manipulations.

Given the diffusion tensor we have the following relations for tensor invariants and tensor elements:

First invariant or trace:

$$I_1 = D_{xx} + D_{yy} + D_{zz} = D_{11} + D_{22} + D_{33} \tag{3.17}$$

Second invariant:

$$I_2 = D_{xx}D_{yy} + D_{xx}D_{zz} + D_{yy}D_{zz} - D_{xy}D_{yx} - D_{xz}D_{zx} - D_{yz}D_{zy} \tag{3.18}$$

$$I_2 = D_{11}D_{22} + D_{11}D_{33} + D_{22}D_{33} \tag{3.19}$$

Third Invariant or determinant:

$$I_3 = D_{xx}\left(D_{yy}D_{zz} - D_{zy}D_{yz}\right) - D_{xy}\left(D_{yx}D_{zz} - D_{zx}D_{yz}\right) - D_{xz}\left(D_{yx}D_{zy} - D_{zx}D_{yy}\right) \tag{3.20}$$

$$I_3 = D_{11}D_{22}D_{33} \tag{3.21}$$

Fourth Invariant:

$$I_4 = I_1^2 - 2I_2 \tag{3.22}$$

$$I_4 = D_{xx}^2 + D_{yy}^2 + D_{zz}^2 + 2D_{xy}D_{yx} + 2D_{xz}D_{zx} + 2D_{yz}D_{zy} \tag{3.23}$$

$$I_4 = D_{11}^2 + D_{22}^2 + D_{33}^2 \tag{3.24}$$

The first invariant is proportional to the sum of the square of the radii of the ellipsoid, the second invariant is proportional to the square of its surface area and the third invariant (determinant) is proportional to the square of its volume. Since computing

the invariants is a mathematical procedure wherein the diffusion constants are either added or multiplied, we need to scale the invariants so they have the units of true diffusion constants [3].

The average, surface, volume and magnitude diffusion coefficients are given by:

$$D_{av} = \frac{I_1}{3} \tag{3.25}$$

$$D_{surf} = \sqrt{\frac{I_2}{3}} \tag{3.26}$$

$$D_{vol} = \sqrt[3]{I_3} \tag{3.27}$$

$$D_{mag} = \sqrt{\frac{I_4}{3}} = \sqrt{3D_{av}^2 - 2D_{surf}^2} \tag{3.28}$$

These orientation independent anisotropies can be related to our scaled invariants and the normalized anisotropy definition is given by [3]:

Fractional Anisotropy

$$FA = \sqrt{\frac{3}{2}}\sqrt{1 - \frac{D_{av}^2}{D_{mag}^2}} = \sqrt{1 - \frac{D_{surf}^2}{D_{mag}^2}} \tag{3.29}$$

Relative Anisotropy

$$RA = \sqrt{\frac{D_{mag}^2}{D_{av}^2} - 1} = \sqrt{2}\sqrt{1 - \frac{D_{surf}^2}{D_{av}^2}} \tag{3.30}$$

Volume Ratio

$$VR = \left(D_{vol} \Big/ D_{av} \right)^3 \tag{3.31}$$

3.5 The Hasan Method

The paper by K. M. Hasan and P. A. Narayanan in 2003 [4] gives an analytical expression that relates commonly used diffusion tensor anisotropy measures obtained from the decoded and diagonalized diffusion tensor to those obtained from the first and

second order moments of the measured diffusion weighted data [4]. RA and FA can then both be computed online which makes it potentially more useful in clinical applications that require realtime execution. RA is related to the mean and standard deviation of the DW moments of the diffusion tensor, and an analytical, expression relating the RA and FA is derived from tensor invariants and given as:

$$FA = \sqrt{1 - I_2 I_4^{-1}} \tag{3.32}$$

$$RA = \sqrt{1 - 3I_2 I_1^{-2}} \tag{3.33}$$

$$FA = \sqrt{3\left[RA^{-2} + 2\right]^{-3}} \tag{3.34}$$

The first and second order moments for the data ADC are given as:

$$m_1 = N^{-1} \sum_{k=1}^{N} ADC_k \tag{3.35}$$

$$m_2 = ADC^t ADC / N \tag{3.36}$$

where N is the number of directions.

Many dimensionless and scale-independent anisotropy measures can be defined from the first and second order moments and then related to the usual FA and RA:

$$Aniso_1 = \sqrt{m_2 / m_1^2 - 1} \tag{3.37}$$

$$Aniso_2 = \sqrt{1 - m_1^2 / m_2} \tag{3.38}$$

The DW based anisotropy measures can be related as:

$$Aniso_2 = \sqrt{1 / \left(1 + Aniso_1^{-2}\right)} \tag{3.39}$$

The relation between RA and $Aniso_1$ after some algebraic reductions is given as:

$$Aniso_1 = \sqrt{0.8} RA \tag{3.40}$$

Using the closed for relation between RA and FA and relating RA to $Aniso_1$, FA can be given as:

$$FA = \sqrt{3.75\left[Aniso_1^{-2} + 2..5\right]^{-1}} \tag{3.41}$$

Since $Aniso_1$ and $Aniso_2$ are related to the mean and standard deviation of diffusion weighted measurements, we can compute FA without tensor decoding and diagonalization [4]. In this thesis from hereon, computing FA maps by the Hasan method without DT will be referred to as the 'Hasan A method', and using DT will be referred to as the 'Hasan B method'.

3.6 The Platonic Variance Method

This method is computationally efficient as it can be programmed directly from the diffusion weighted images. This method uses gradient acquisition schemes, based on platonic solids: the icosahedric scheme $(N = 6)$, the dodecahedric scheme $(N = 10)$ and their combinations-translating to acquiring DT-MRI data in 6 and 10 directions respectively. This scheme was put forth by Erik Akkerman in 2003 [5]. It is based on the relation that the average of the diffusion tensor Eigen values equals the average of the measured ADC and the variance of the Eigen values equals 5/2 times the variance of the diffusion coefficients:

$$\overline{\lambda} = \overline{ADC} \tag{3.42}$$

$$Var\lambda = \frac{5}{2} Var(ADC) \tag{3.43}$$

Since this property has been verified only for icosahedrons and dodecahedron which are platonic solids and their combinations, this method of computing FA maps is called the Platonic Variance Method. It provides compact expressions for anisotropy measures, directly in terms of images without involving tensor elements or Eigen value computation. The tensor calculation procedure can be very time consuming and computationally expensive. Additionally many MRI scanners do not have the software to these calculations which have to be run on a separate dedicated workstation. Using the

Platonic Variance Method the FA map is calculated as simple “one-step” functions of the acquired diffusion weighted images [5].

Using diffusion tensor method the FA map is given by:

$$FA = \sqrt{\frac{3}{2}}\sqrt{\frac{Var\lambda}{\overline{\lambda^2}}} \tag{3.44}$$

From earlier computations we can relate the mean and variance of Eigen values to the mean and variance of ADC maps:

$$\overline{\lambda} = \overline{ADC} \tag{3.45}$$

$$Var\lambda = \frac{5}{2}Var(ADC) \tag{3.46}$$

The FA map in terms of the *ADCs* is given by:

$$FA = \sqrt{\frac{3}{2}}\sqrt{\frac{\frac{5}{2}Var(ADC)}{\frac{5}{2}Var(ADC) + \left(\overline{ADC}\right)^2}} \tag{3.47}$$

Also:
$$\overline{ADC} = \overline{\lambda} = \frac{\ln S_0 - \overline{\ln S}}{b} \tag{3.48}$$

By the above calculations we compute the FA as:

$$FA = \sqrt{\frac{3}{2}}\sqrt{\frac{\frac{5}{2}Var(\ln S)}{\frac{5}{2}Var(\ln S) + \left(\ln S_0 - \overline{\ln S}\right)^2}} \tag{3.49}$$

where $\overline{\ln S}$ and $Var(\ln S)$ are the average and variance of $\ln S_j$, $j = 1.....23$. Thus we observe that FA can be computed directly from the weighted images independent of tensor elements and b-value.

RA can be computed as:

$$RA = \frac{\sqrt{Var\,\lambda}}{\bar{\lambda}} = \frac{\sqrt{\frac{5}{2}Var(\ln S)}}{\ln S_0 - \overline{\ln S}} \tag{3.50}$$

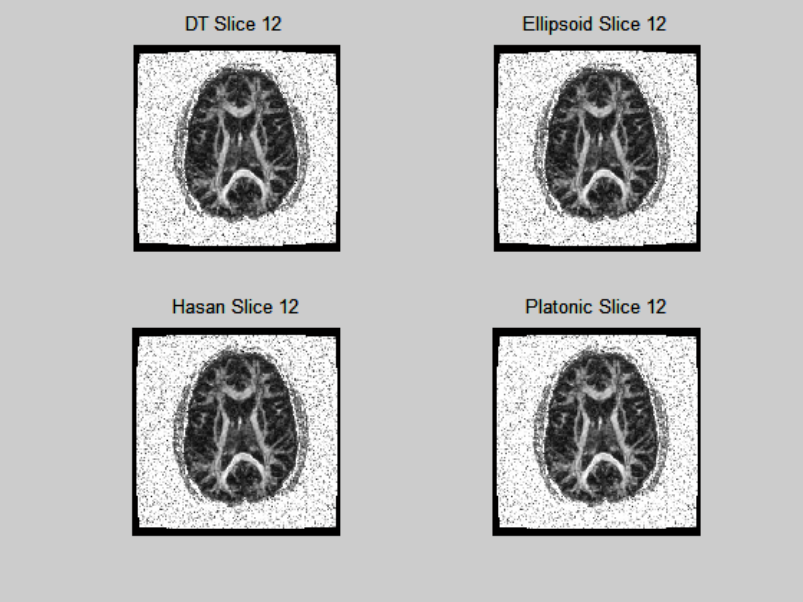

Figure 3.1 FA maps in an axial slice of human brain using the four methods

Chapter 4: Noise and Error Propagation

Noise is an inherent problem in diffusion weighted images. There are two major sources of noise in DTI measurements:

i. Electromagnetic noise in the body due to movement of charged particles
ii. Small anomalies in the measurement electronics, which depend on the size of the RF coil and the bandwidth of the pulse sequence.

Noise in image data acquisition produces errors in the calculated quantities for all methods. Random variations in these quantities complicate the analysis and interpretation of DTI data [20], [22].

The error in anisotropy index calculations is due to the noise in the raw DTI data. Both the noise and the selected diffusion weighting scheme propagate through the diffusion tensor imaging computational chain into the variances of the diffusion tensor elements and then into the errors in the anisotropy indices. Depending on the *b* values, the number of diffusion gradient directions *N*, and diffusion weighting gradient scheme, the noise in the DW images could propagate into variances or other statistics computed on the diffusion tensor elements [6].

4.1 Computing Error Propagation in DTI Parameters

For the two parameter case, we refer to the work of Poonawalla and Zhou [6] to investigate error propagation. Let *x* be a given descriptor for a type of anisotropy, for example: FA, RA, VR etc. Let *u* and *v* be the parameters used to determine *x*, for example: D_{surf} , D_{mag} , D_{vol} . These are the for the variance measure the error propagation is given as:

$$\sigma_x^2 = \sigma_u^2\left(\frac{\partial x}{\partial u}\right)^2 + \sigma_v^2\left(\frac{\partial x}{\partial v}\right)^2 + 2\sigma_{uv}^2\left(\frac{\partial x}{\partial u}\right)\left(\frac{\partial x}{\partial v}\right) \tag{4.1}$$

Since the covariance terms [last term of the equation above] are significantly smaller than the variance terms, we can disregard them and on applying the above formula, the error propagation in tensor shape invariants is computed. The error propagation σ_{FA} for FA can be computed as follows:

$$FA = \sqrt{1 - \frac{D_{surf}^2}{D_{mag}^2}} \tag{4.2}$$

Taking the partial derivative of FA with respect to D_{surf} and D_{mag} results in the following equation:

$$\frac{\partial FA}{\partial D_{surf}} = \frac{1}{2}(FA)^{-1}\left(-2D_{surf}D_{mag}^{-2}\right) = -\frac{1}{FA}\cdot\frac{D_{surf}}{D_{mag}^2}$$

$$\frac{\partial FA}{\partial D_{mag}} = \frac{1}{2}(FA)^{-1}\cdot\left(2D_{mag}^{-3}D_{surf}^2\right) = -\frac{1}{FA}\cdot\frac{D_{surf}^2}{D_{mag}^3}$$

The variance in FA can now be expressed using these terms:

$$\sigma_{FA}^2 = \frac{1}{(FA)^2}\left[\left(\frac{D_{surf}}{D_{mag}^2}\right)\sigma_{surf}^2 + \left(\frac{D_{surf}^2}{D_{mag}^3}\right)^2\sigma_{mag}^2\right]$$

$$\sigma_{FA}^2 = \left(\frac{1}{FA}\cdot\frac{D_{surf}}{D_{mag}}\right)^2\left[\sigma_{surf}^2 + \left(\frac{D_{surf}}{D_{mag}}\right)^2\sigma_{mag}^2\right] \tag{4.3}$$

For the three parameter case we can extend the variance expression to obtain:

$$\sigma_x^2 = \sigma_u^2\left(\frac{\partial x}{\partial u}\right)^2 + \sigma_v^2\left(\frac{\partial x}{\partial v}\right)^2 + \sigma_w^2\left(\frac{\partial x}{\partial w}\right)^2 + 2\sigma_{uv}^2\left(\frac{\partial x}{\partial u}\right)\left(\frac{\partial x}{\partial v}\right) + 2\sigma_{uw}^2\left(\frac{\partial x}{\partial u}\right)\left(\frac{\partial x}{\partial w}\right) + 2\sigma_{vw}^2\left(\frac{\partial x}{\partial v}\right)\left(\frac{\partial x}{\partial w}\right) \tag{4.4}$$

This approach for the computation of the error propagation has been further extended in this thesis. Error propagation has been computed in other scalar indices such as trace, volume ratio, anisotropy index, ultimate anisotropy. The results are summarized in Table 4.1 below.

Computing error propagation in a three parameter case for example the error σ_{AI} of the anisotropy index can be expressed as:

$$AI = 2\left(3D_{av}^2 - 2D_{surf}^2 - D_{vol}^2\right) \tag{4.5}$$

Taking the partial derivative of AI with respect to D_{av}, D_{surf} and D_{vol}

$$\frac{\partial AI}{\partial D_{av}} = 12D_{av}$$

$$\frac{\partial AI}{\partial D_{surf}} = -8D_{surf}$$

$$\frac{\partial AI}{\partial D_{vol}} = -4D_{vol}$$

The variance can be expressed using these terms:

$$\sigma_{AI}^2 = \sigma_{av}^2\left(\frac{\partial AI}{\partial D_{av}}\right)^2 + \sigma_{surf}^2\left(\frac{\partial AI}{\partial D_{surf}}\right)^2 + \sigma_{vol}^2\left(\frac{\partial AI}{\partial D_{vol}}\right)^2$$

$$\sigma_{AI}^2 = 144D_{av}^2\sigma_{av}^2 + 64D_{surf}^2\sigma_{surf}^2 + 16D_{vol}^2\sigma_{vol}^2 \tag{4.6}$$

The errors in VR, Trace, and Ultimate Anisotropy are derived in the same manner as equations [4.3] and [4.6].

Table 4.1 Variances in Error Propagation of the Various DTI Parameters

Parameter	**Error Propagation**
Fractional Anisotropy $FA = \sqrt{1 - \frac{D_{surf}^2}{D_{mag}^2}}$	$\sigma_{FA}^2 = \left(\frac{1}{FA}\cdot\frac{D_{surf}}{D_{mag}}\right)^2\left[\sigma_{surf}^2 + \left(\frac{D_{surf}}{D_{mag}}\right)^2\sigma_{mag}^2\right]$
Relative Anisotropy $RA = \sqrt{2}\sqrt{1 - \frac{D_{surf}^2}{D_{av}^2}}$	$\sigma_{RA}^2 = \left(\frac{2}{RA}\cdot\frac{D_{surf}}{D_{av}^2}\right)^2\left[\sigma_{surf}^2 + \left(\frac{D_{surf}}{D_{av}}\right)^2\sigma_{av}^2\right]$

Volume Ratio $VR = \left(D_{vol} \middle/ D_{av} \right)^3$	$\sigma_{VR}^2 = \frac{9D_{vol}^4}{D_{av}^6}\left[\sigma_{vol}^2 + \left(\frac{D_{vol}}{D_{av}} \right)^2 \sigma_{av}^2 \right]$
Trace $D_{av} = \frac{1}{3}\left(D_{xx} + D_{yy} + D_{zz} \right)$	$\sigma_{trace}^2 = \sigma_{xx}^2 + \sigma_{yy}^2 + \sigma_{zz}^2$
Anisotropy index $AI = 2\left(3D_{av}^2 - 2D_{surf}^2 - D_{vol}^2 \right)$	$\sigma_{AI}^2 = 144D_{av}^2\sigma_{av}^2 + 64D_{surf}^2\sigma_{surf}^2 + 16D_{vol}^2\sigma_{vol}^2$
Ultimate Anisotropy UA_{surf} $UA_{surf} = \sqrt{\left(\frac{D_{surf}}{D_{av}} - 1 \right)^2}$	$\sigma_{UAsurf}^2 = \frac{1}{D_{av}^2}\left[\sigma_{surf}^2 + \left(\frac{D_{surf}}{D_{av}} \right)^2 \sigma_{av}^2 \right]$
Ultimate Anisotropy UA_{vol} $UA_{vol} = \sqrt{\left(\frac{D_{vol}}{D_{av}} - 1 \right)^2}$	$\sigma_{UAvol}^2 = \frac{1}{D_{av}^2}\left[\sigma_{vol}^2 + \left(\frac{D_{vol}}{D_{av}} \right)^2 \sigma_{av}^2 \right]$
Ultimate Anisotropy $UA_{vol,surf}$ $UA_{vol,surf} = \sqrt{\left(\frac{D_{vol}}{D_{surf}} - 1 \right)^2}$	$\sigma_{UAvol,surf}^2 = \frac{1}{D_{surf}^2}\left[\sigma_{vol}^2 + \left(\frac{D_{vol}}{D_{surf}} \right)^2 \sigma_{surf}^2 \right]$
Mean Radius $D_{av} = \frac{1}{3}\left(D_{xx} + D_{yy} + D_{zz} \right)$	$\sigma_{av}^2 = \frac{1}{9}\left(\sigma_{xx}^2 + \sigma_{yy}^2 + \sigma_{zz}^2 \right)$
Surface Area $D_{surf} = \sqrt{\frac{1}{3}\left(\begin{matrix} D_{xx}D_{yy} + D_{xx}D_{zz} + D_{yy}D_{zz} - \\ D_{xy}^2 - D_{xz}^2 - D_{yz}^2 \end{matrix} \right)}^{1/2}$	$\sigma_{surf}^2 = \frac{1}{\left(6D_{surf} \right)^2}\left[\begin{matrix} \left(D_{yy} + D_{zz} \right)^2 \sigma_{xx}^2 + \left(D_{xx} + D_{zz} \right)^2 \sigma_{yy}^2 \\ + \left(D_{xx} + D_{yy} \right)^2 \sigma_{zz}^2 + 4D_{xy}^2\sigma_{xy}^2 \\ + 4D_{xz}^2\sigma_{xz}^2 + 4D_{yz}^2\sigma_{yz}^2 \end{matrix} \right]$
Magnitude $D_{mag} = \sqrt{\frac{1}{3}\left(\begin{matrix} D_{xx}^2 + D_{yy}^2 + D_{zz}^2 + \\ 2D_{xy}^2 + 2D_{xz}^2 + 2D_{yz}^2 \end{matrix} \right)}^{1/2}$	$\sigma_{mag}^2 = \frac{1}{\left(3D_{mag} \right)^2}\left[\begin{matrix} D_{xx}^2\sigma_{xx}^2 + D_{yy}^2\sigma_{yy}^2 + D_{zz}^2\sigma_{zz}^2 \\ + 4D_{xy}^2\sigma_{xy}^2 + 4D_{xz}^2\sigma_{xz}^2 + 4D_{yz}^2\sigma_{yz}^2 \end{matrix} \right]$

4.2 Computing MSE and SNR

Mean square error (MSE) is defined as the average of the square of the difference between the sampled and original image. The higher the value of MSE, the greater is the error in the sampled image. In this thesis, MSE has been used to evaluate the results of FA calculations in simulated and real human brain DTI data.

Consider an original image X of matrix size $N \times N$. Let Y be the sampled image of the same size. The MSE between X and Y can be computed as follows:

$$MSE = \frac{1}{N \times N} \sum_{i=1}^{N} \sum_{j=1}^{N} \left[X(i,j) - Y(i,j) \right]^2 \tag{4.7}$$

The term Signal-to-Noise-Ratio, often abbreviated as SNR or S/N, is an engineering term for the ratio between the magnitude of the signal (meaningful information) and the magnitude of the background (unwanted) noise. Since many signals have a very wide dynamic range, SNR's are often expressed in the terms of a logarithmic decibel scale. It is preferred to have a high SNR, and hence a smaller associated MSE.

$$SNR = 10 \log_{10} \frac{h^2}{MSE} (db) \tag{4.8}$$

where h is the maximum intensity value (usually $h = 255$ for an 8-bit image).

SNR in medical imaging can be different to the expression above – the difference occurs in how the background noise is defined, and hence the calculations can differ. It is well known that quantitative anisotropy measurements derived from the diffusion tensor are extremely sensitive to noise contamination [20]. The level of noise in the diffusion tensor imaging (DTI) experiment is usually measured from some estimate of the SNR in the component diffusion-weighted (DW) images. SNR is used to describe the relative contributions to a detected signal of the true signal and the superimposed signal ("background noise") - a criterion for image quality [7].

SNR can be measured by recording the mean value of a small region of interest (ROI) (R_A as shown in Fig. 4.1) placed in an homogeneous area of the tissue with high signal intensity (e.g. white matter) and the standard deviation of the background ROI (R_B as shown in Fig. 4.1) placed outside the object in the image background (avoid ghosting or aliasing).

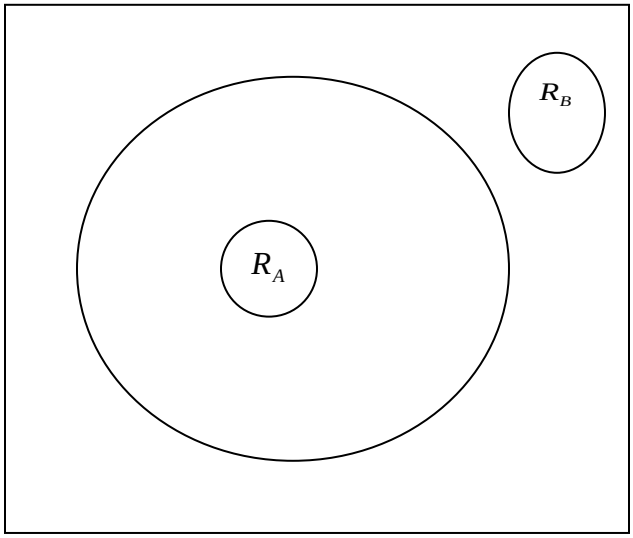

Figure 4.1 Diagrammatic representation of the regions to compute SNR

$$\text{SNR} = \frac{\text{Mean signal in region } R_A}{\text{Standard deviation of background noise (region } R_B)} \quad (4.9)$$

A common method that is used to improve SNR is to average several measurements of the sampled data. The SNR can also be improved by sampling larger volumes (increasing the field of view and slice thickness but coming with a cost of a corresponding loss of spatial resolution) or by increasing the magnetic field. Surface coils can also be used to improve the SNR in the tissue of interest. SNR increases in proportion to the square root of the number of scan encodings. SNR decreases with field of view squared and wider bandwidths [7].

4.3 Filtering and Improvements in Image Quality

The images obtained from the MRI scanner contain a lot of noise in the form of random, unwanted RF energy picked up from the patient's body. It is essential to use robust methods to minimize or eliminate the noise in order to increase the reliability of the data.

4.3.1 Threshold Based Filtering

Let I be an $N \times N$ image with i and j denoting the co-ordinates of individual voxels in the image. Using the thresholding method on the source images we remove the neighboring noise:

$$I(i,j) = \begin{cases} 0 & if \quad I(i,j) \le \tau \quad i = 1...N, j = 1....N \\ I(i,j) & otherwise \end{cases} \tag{4.10}$$

where τ is a threshold.

This thresholding or masking procedure retains the central part of the image while eliminating all the surrounding noise. A histogram of the signal intensities in the source images is plotted and depending on the peak in the histogram we select τ so as to eliminate all the noise in the background. We set all the pixels to the left hand side of the peak to zero.

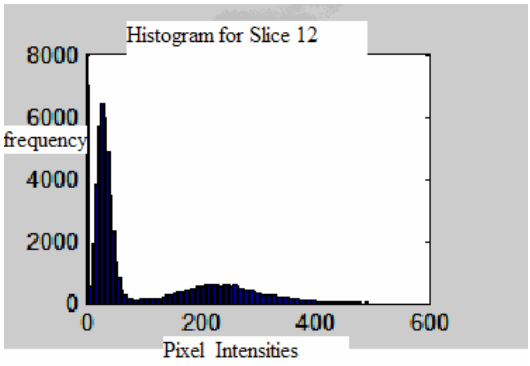

Figure 4.2 Histogram plot for slice 12

4.3.2 Median Filtering

Median filtering is a simple and very effective noise removal filtering process. When performing median filtering, the median value of all pixels in a selected neighborhood (mask, template, window). The median value **m** of a population (set of pixels in a neighborhood) is that value in which half of the population has smaller values than **m**, and the other half has larger values than **m**. This class of filter belongs to the class of edge preserving smoothing filters which are non-linear filters. These filters smooth the data while preserving the small and sharp details or high spatial frequencies.

Figure 4.2 compares the results of thresholding and median filtering. The FA maps in these results are obtained for real MRI data from a human brain sampled with 26 slices. Unfiltered and filtered source images are used to calculate FA maps slices 11, 12 (from the center of the sampled brain volume) and calculated using the DT method are shown.

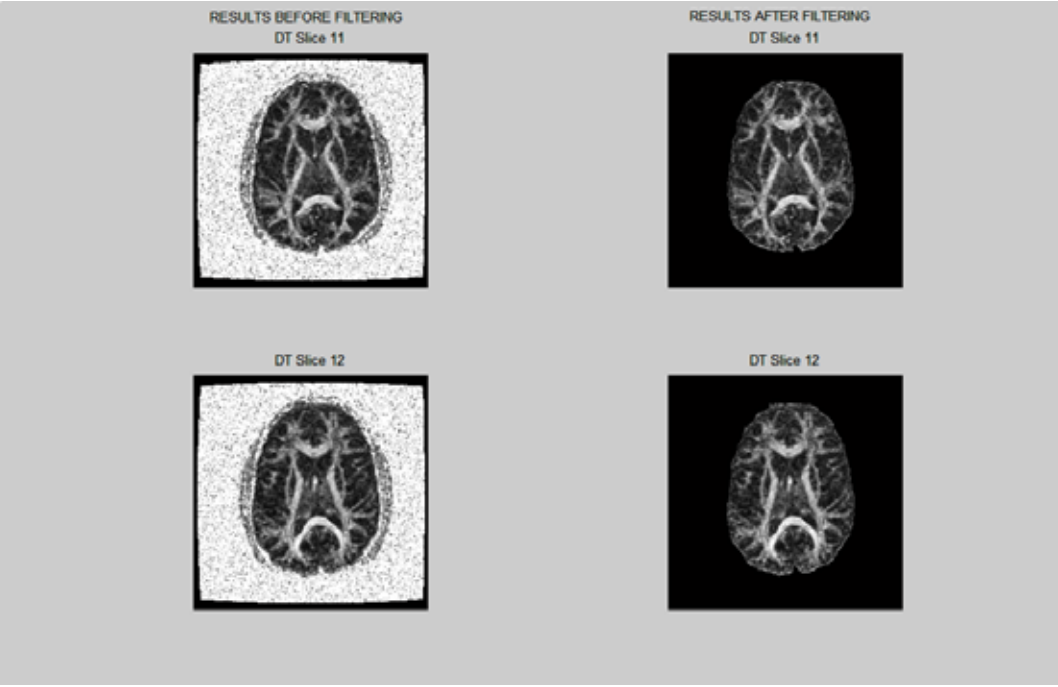

Figure 4.3 FA maps before (left) and after (right) filtering in two axial slices of the brain

4.4 Intervoxel Coherence Methods

Section 4.3 dealt with filtering the source or intensity images by thresholding and median filtering. In this section noise removal following the computation of the FA maps, which helps improve the visual quality of the image is described. The pixel values are changed depending on neighboring pixels by the averaging and neighborhood difference method; hence we call this intervoxel coherence. A 3×3 or 5×5 matrix is selected and the center pixel is varied according to its neighborhood using the algorithms described in the following two subsections.

4.4.1 Computing Average FA maps

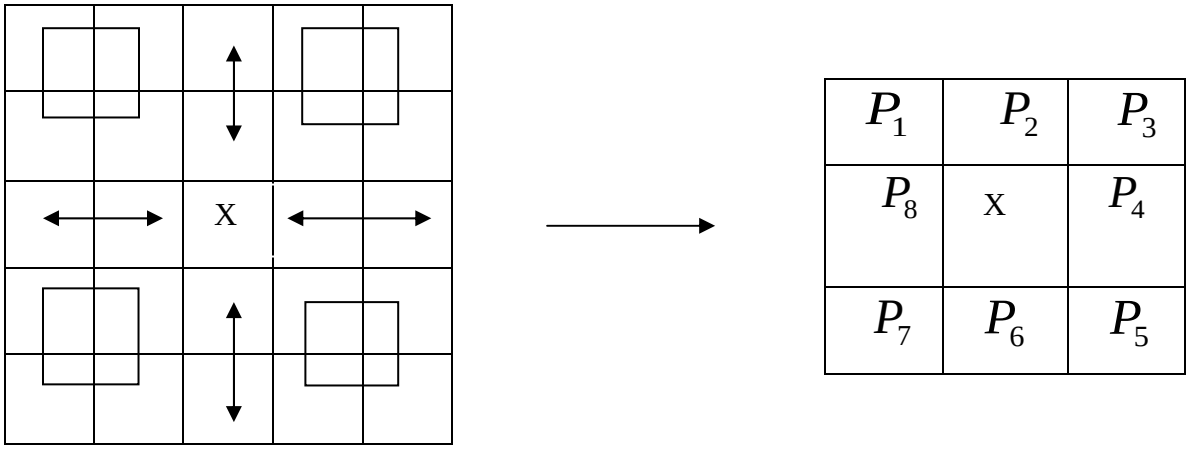

Figure 4.4 Averaging method for FA maps

In this method we scan the entire image using a 5×5 pixel matrix. The average of four pixels at the four corners of the matrix is taken to obtain P_1, P_3, P_5, P_7. The vertical pixels are averaged to obtain P_2, P_6 , whereas averaging the horizontal pixels yields P_4, P_8. Essentially this maps a 5×5 matrix to a 3×3 matrix. The method is explained schematically in the Figure 4.4.

If we consider a unit square, the distance for all diagonal elements is 1.414 and that of the vertical and horizontal elements is 1. Thus we can assign weights c, to the entries in the 3×3 matrix as follows:

$$\begin{aligned} c_1 &= c_3 = c_5 = c_7 = 1/\sqrt{2} \\ c_2 &= c_4 = c_6 = c_8 = 1 \end{aligned} \tag{4.11}$$

We compute FA_a using the formula:

$$FA_a = \frac{\sum_{i=1}^{8} P_i c_i}{\sum_{i=1}^{8} c_i} \tag{4.12}$$

4.4.2 Neighborhood Difference

P_1	P_2	P_3
P_8	X	P_4
P_7	P_6	P_5

Figure 4.5 A 3×3 size matrix for neighborhood difference

This method involves computing the difference between the center pixels and its eight neighbors of a 3×3 size matrix and assigning a weighting coefficient to the neighborhood pixel depending on the magnitude of the difference. The algorithm for this method is as shown below:

1. Compute $\Delta D_i = |X - P_i| \quad \forall i = 1,2,.....,8$ where X is the center pixel, $P_1, P_2, ..., P_8$ are the eight neighbors specified in a clockwise manner and ΔD_i

is the difference in the signal intensity between the center and the i^{th} neighborhood pixel.

2. Set the coefficient vector as $c = \begin{bmatrix} 1 & 0.9 & 0.8 & 0.7 & 0.6 & 0.5 & 0.4 & 0.3 \end{bmatrix}$.
3. Sort ΔD_i values in the ascending order and assign a maximum coefficient to the minimum ΔD_i value.
4. Compute FA_d using:

$$FA_d = \frac{\sum_{i=1}^{8} c_i \Delta D_i}{\sum_{i=1}^{8} c_i} \tag{4.13}$$

4.4.3 Combining Averaging and Neighborhood Difference

Here we compute FA maps by combining the averaging method with pixel differences using a simple average:

$$FA_c = \frac{FA_a + FA_d}{2} \tag{4.14}$$

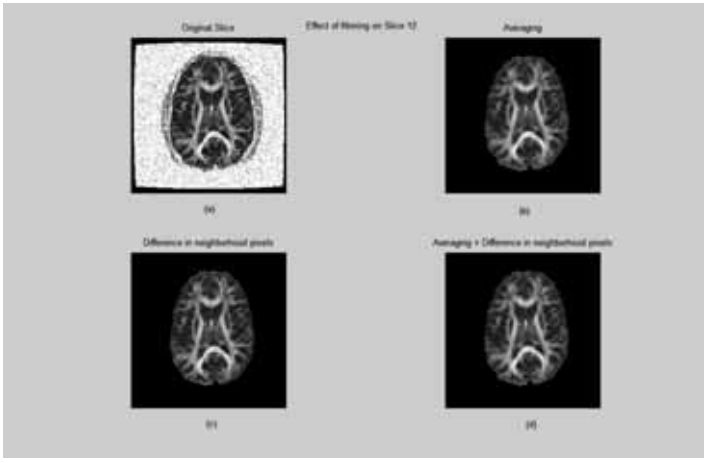

Figure 4.6: Effects of intervoxel coherence on an axial slice using the DT method (a) Original slice (b) Slice after averaging method, FA_a (c) Slice after neighborhood difference, FA_d (d) Slice after combining averaging and neighborhood difference FA_c

Intervoxel coherence generates FA maps of a better visual quality when observed with naked eye. We observed that the averaging method gives better results as compared to the neighborhood difference method in terms of computational efficiency and MSE as shown in the next section.

Chapter 5: Experiments and Results

5.1 Simulation

5.1.1 Simulation Environment

To evaluate the performance of the various methods for computing DTI parameters, we performed experiments using both human brain MR images and simulated digital data sets. The experiments were performed on an Inspiron 5160 Intel Pentium 4 Processor 518 (2.80 GHz) with 512 MB RAM and 60 GB Ultra ATA Hard Drive in a laptop PC. The software platform used was MATLAB 6.5.

5.1.2 Simulation Assumptions and Simulated Data

Simulated data were generated using a matrix size 128×128 in the form of squares, circles, overlapping squares and circles and horizontal and vertical bars on circles. The diffusion tensor coefficients were chosen depending on the type of data to be obtained. We chose a set of diffusion tensor as shown in table 5.1 to obtain four distinct rings in the simulated data. The gradients in six different directions were selected, with the following directional cosines: $\left(\pm\sqrt{2}/2,\ 0,\ \sqrt{2}/2\right)$, $\left(0,\ \sqrt{2}/2,\ \pm\sqrt{2}/2\right)$, $\left(\pm\sqrt{2}/2,\ \sqrt{2}/2,\ 0\right)$. These were taken from the standard GE pulse sequence. This generated a set of 8-bit source images shown in Figure 5.1 which provided an input to the programs that generated FA maps using the DT, Hasan, Ellipsoid and Platonic Variance methods. A number of computations were performed on simulated and real MRI data i.e. filtering, added noise, and computed MSE and BIAS of FA maps as well as the computational efficiency of each of the method. Results from the simulated and real data were then compared. Using simulated data with a relatively simple form i.e. with diffusion tensor coefficients either in the *x, y, z* direction we could validate our methods for the implemented display of the directions as color coded FA maps and check the FA calculations.

5.1.3 Results with Simulated Data

We used the set of diffusion tensors as shown in Table 5.1 to generate six data sets of matrix size 128×128 as shown in Figure 5.1.

Table 5.1: Diffusion tensor coefficients for simulated data

Directions	D1 (Outer Circle)	D2 (Second Outer Circle)	D3 (Third Outer Circle)	D4 (Center Circle)
X	1	0.2	0	0
Y	0	0.5	1	0.3
Z	0.4	1	0.7	1
XY	0	0	0	0
YZ	0	0	0	0
XZ	0	0	0	0

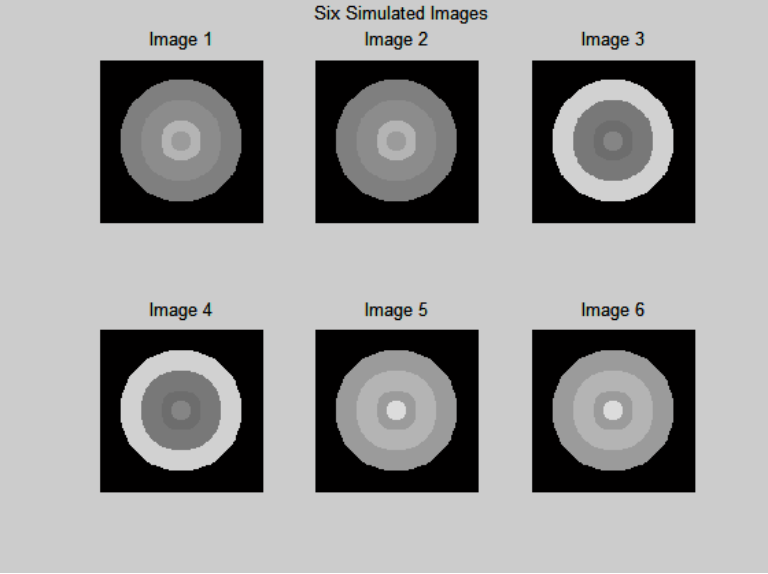

Figure 5.1 Simulated source images

The algorithms for the four methods of calculating the FA maps gave results as shown in Table 5.2. Each row of results is for the same pixel value in all the FA maps using the different methods. These pixel values correspond to *D1, D2, D3, and D4* from outer to inner rings respectively. FA values will always range between 0 to 1 where 0 indicates isotropic diffusion and 1 indicates complete anisotropy. Similar results were obtained using the DT, the Ellipsoid and the Hasan B method (with DT).

Table 5.2 FA values for simulated data using the four methods

True Value	DT method	Ellipsoid	Hasan		Platonic Variance
			A (w/o DT)	B (with DT)	
0.80943	0.80943	0.80943	0.69978	0.80943	0.74271
0.61632	0.61632	0.61632	0.51216	0.61632	0.55149
0.72815	0.72815	0.72815	0.61807	0.72815	0.66045
0.85133	0.85133	0.85133	0.74379	0.85133	0.7863

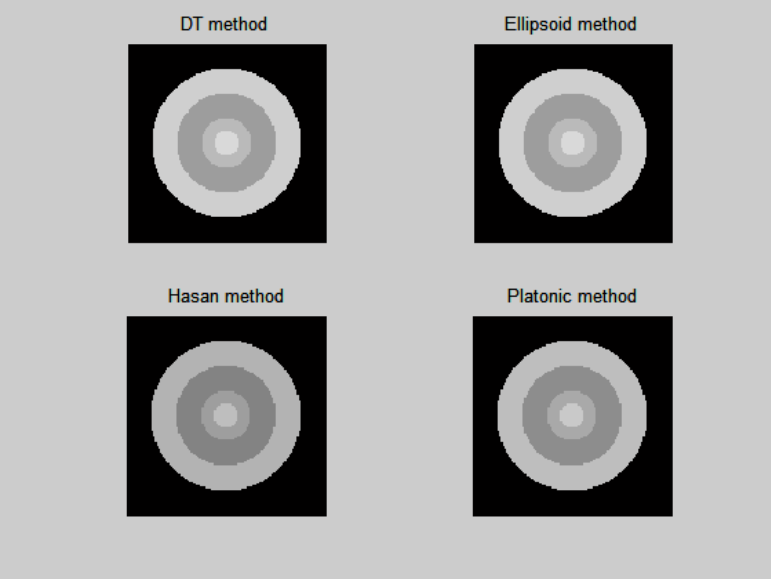

Figure 5.2 FA maps for simulated data using the four methods

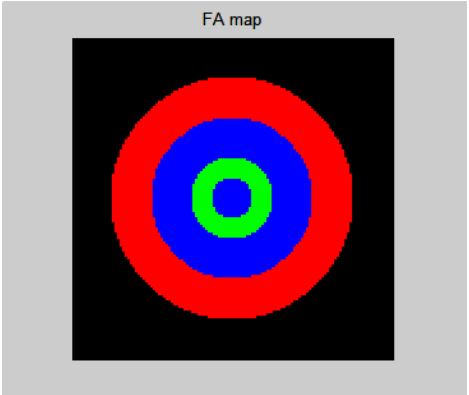

Red: X direction dominates
Green: Y direction dominates
Blue: Z direction dominates

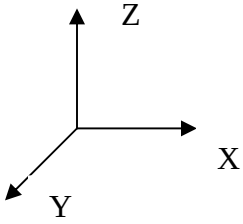

Figure 5.3 Directional FA map for simulated data

As observed from the FA map shown in Figure 5.3, the outermost red ring indicates dominant diffusion is in the *x* direction, i.e. corresponding to *D1* which has a

maximum coefficient in the *x* direction. Thereafter, since *D2* has a maximum coefficient in *z* direction, we observe a blue ring in the image indicating that the directional diffusion is in *z* direction. Thus from visual inspection of these results, it appears that the simulated data were useful in checking the correctness of the computations and validating the methods.

As stated earlier, we simulated structures such as squares, circles, overlapping squares and circles and horizontal and vertical bars on circles using the same method and parameters. In terms of direction, all the four methods produced the same results. For given simulated data we generated the expected directional FA maps as shown in Figure 5.4.

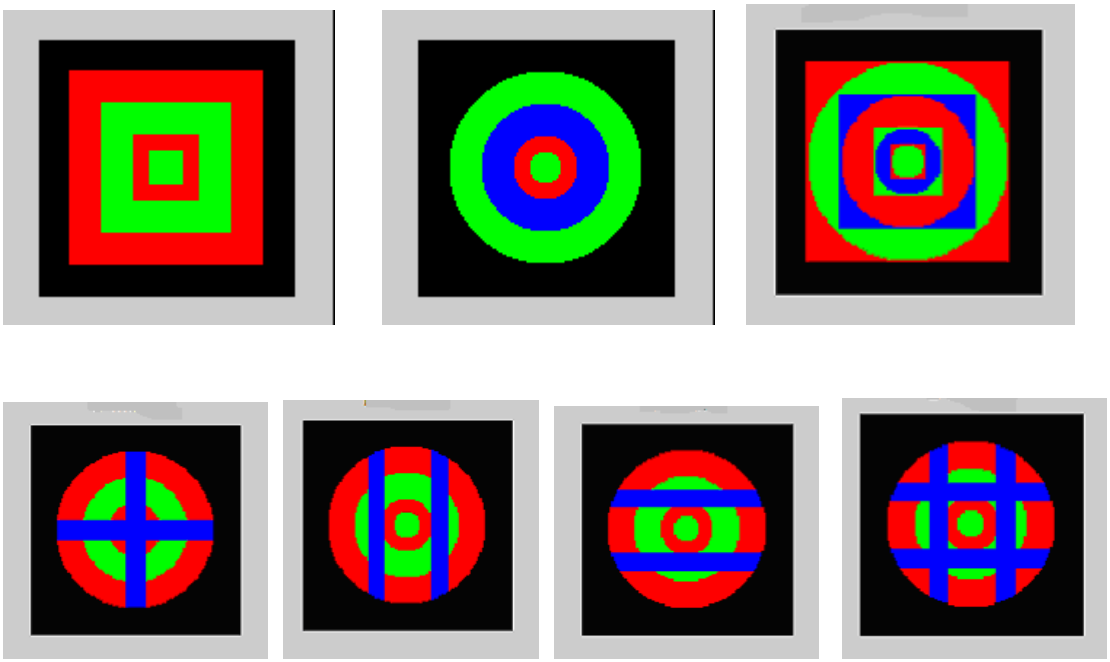

Red: X direction
Green: Y direction
Blue: Z direction

Figure 5.4 FA maps obtained using different simulated data

5.1.4 Results with Addition of Noise

To test the robustness of the four methods in the presence of noise, we added Gaussian noise with *mean* = 0 and variance increasing from 0.001 to 0.005, in steps of 0.001, to the simulated data.

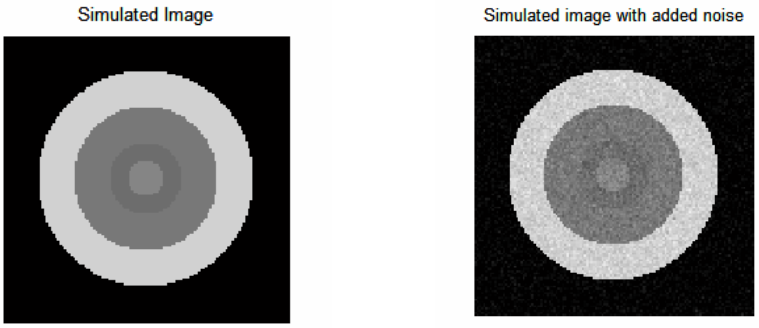

Figure 5.5: Original simulated image (left) and simulated image with added Gaussian noise (right) of variance = 0.002

We obtained plots for Mean Square Error and Average difference of FA maps (sometimes called the BIAS [16]) for simulated data. The FA map obtained from the original source images was taken as a reference to compute MSE of the FA map generated from the noisy images. Plots for the DT, the Ellipsoid and the Hasan B (with DT) overlap each other as they gave almost the same results. Hasan A (without DT) showed minimum noise robustness.

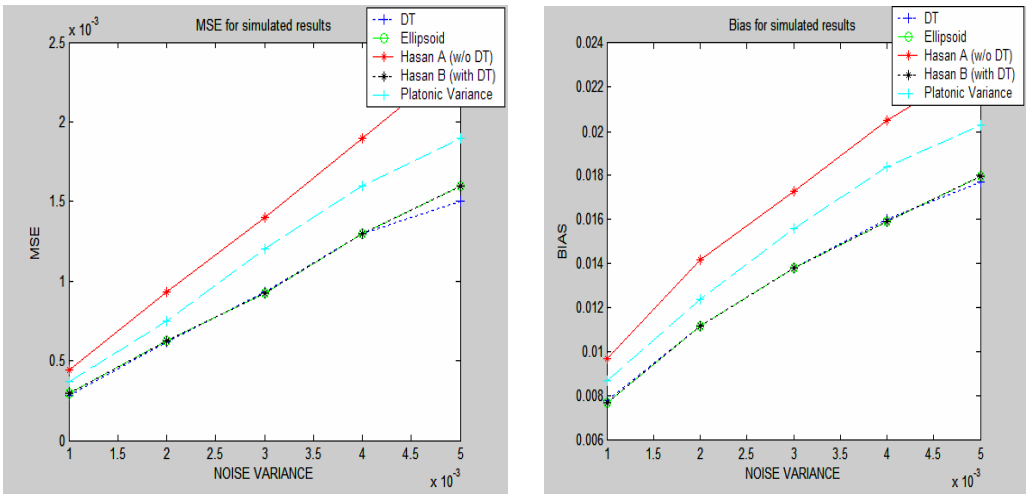

Figure 5.6: Plot of MSE and BIAS of FA v/s noise variance for simulated data

5.2 Human Brain MRI Data

5.2.1 Human Brain MRI Data Acquisition and Data Analysis Strategy

To test the various DTI methods, an MRI experiment was performed on a 3.0 Tesla General Electric Medical Systems Horizon LX MRI scanner at the Center of Advanced Imaging at WVU using a standard quadrature head coil. Sets of MRI and DTI were obtained from a healthy 25 year old male subject who consented to participate in a study approved by the Institutional Review Board at West Virginia University. The MRI scanner featured a gradient system capable of 40 mT/m gradient amplitude and a slew rate of 400 *T/m/second*. To acquire the DTI data, a standard spin echo planar imaging tensor pulse sequence was used. The b value was chosen to be 1000 s/mm^2 and a diffusion scheme with $N = 6$ directions. We used three pairs of vectors with the following directional cosines: $\left(\pm\sqrt{2}/2,\ 0,\ \sqrt{2}/2\right)$, $\left(0,\ \sqrt{2}/2,\ \pm\sqrt{2}/2\right)$, $\left(\pm\sqrt{2}/2,\ \sqrt{2}/2,\ 0\right)$ selected from the standard GE pulse sequence. The imaging sequence parameters were TE = 20 ms, TR between the acquisitions = 9 s, field of view (FOV) = 24 cm, phase FOV = 1, axial slice thickness = 4mm, interslice gap = 1mm, 26 slices and image matrix size = 128×128. Data were acquired to cover the whole brain. Four sets of these acquisitions were taken with the same parameters but NEX was varied as $NEX = 1,2,3,4$. The total scan time was around 5 minutes for each data set for our data acquisition. For each set of data, one acquisition of unweighted images was taken at $b = 0$ s/mm^2. For any acquisition, the total number of images can be obtained from the number of directions, slices in each direction and the number of unweighted images:

*Total Number of images = Number of directions*Number of slices in each direction + Unweighted images*

= (n directions + 1) n slices*

$$182 = (6 \times 26) + 26$$

As described for the simulated data, FA maps were computed from the reconstructed brain DTI data using the DT, Hasan, Ellipsoid and Platonic Variance methods. All other calculations like filtering these maps, adding noise, computing MSE and bias, performed for simulated data were repeated for the human data.

5.2.2 Results with Human Structural MRI Data

The MRI images obtained from the MRI scanner were byte swapped using a routine implemented in C to generate the source images [see Appendix Figure A1]. As mentioned in the earlier Section 5.2.1, a whole brain data set consisting of 26 slices were taken in each direction, but the 26^{th} slice had no brain coverage; hence we have not obtained a source image for that and for every 26^{th} slice in all the other directions. These source images were used as the input for the programs to generate FA maps.

The corresponding FA maps were generated using source images when $NEX = 4$, with DT method for each of the 25 slices in 6 different directions are as shown in the Figure 5.7

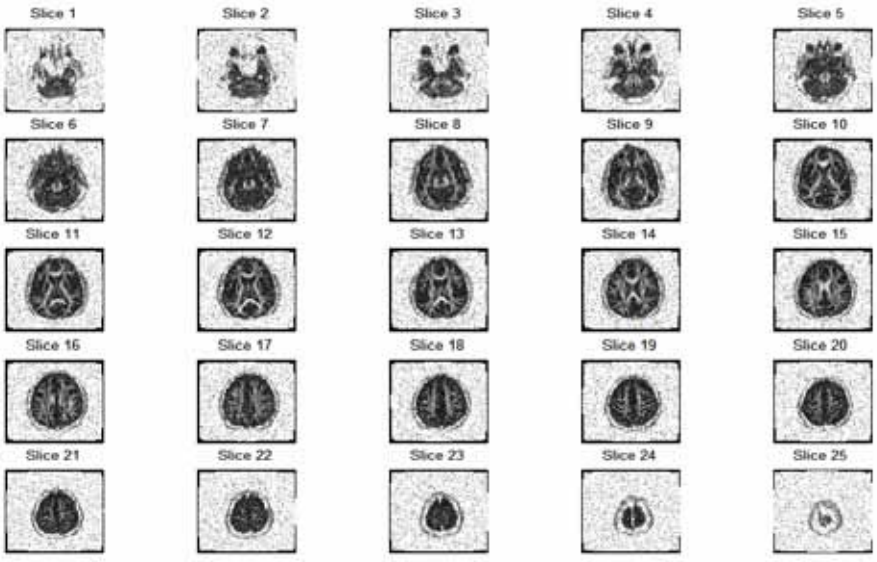

Figure 5.7 FA maps using DT with $NEX = 4$

The FA maps from all the four different methods are shown in Figure 5.8 for source images with $NEX = 4$. It can be observed that all four methods give the same visual results. The DT and Ellipsoid give nearly the same FA values. We have generated FA maps for all 25 slices using the four methods. However, we have displayed only slices 10-13 for all the methods as the major portion of the brain and the white matter tracts are observed in these slices. FA maps for source images with $NEX = 1,2,3$ for slices 10-13 for all four methods are shown in the Appendix (Figures A8, A9, and A10 respectively).

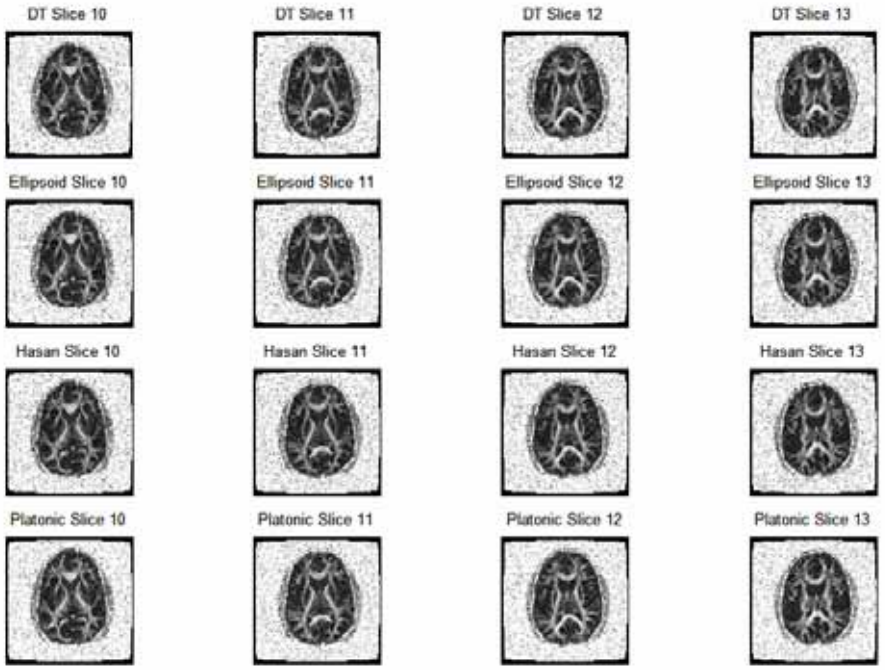

Figure 5.8 FA maps using the four methods with $NEX = 4$

5.2.3 Results with Addition of Noise

To test the robustness of the four methods in the presence of noise, we added Gaussian noise with $mean = 0$ and variance increasing from 0.001 to 0.005, in steps of 0.001, to the set of source images of human brain MRI data. Figure 5.9 shows a slice of human brain before and after addition of Gaussian noise.

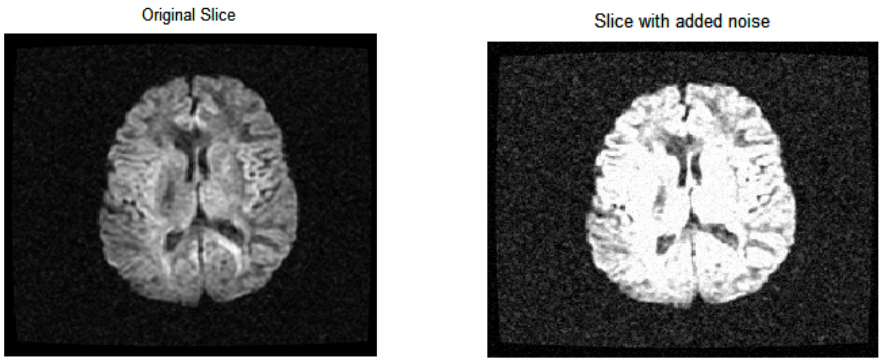

Figure 5.9: Original brain slice (left) and slice with added Gaussian noise (right) of variance = 0.002

Thereafter we computed the Average difference of the FA maps (sometimes called the BIAS [16]) as well as the Mean Square Error (MSE) for slice 3 and slice 12 with NEX = 4. The results are as shown in Figure 5.10 and Figure 5.11 respectively. The plots for Diffusion Tensor, Diffusion Ellipsoid and Hasan A (with DT) lie on top of one another. Hasan A gives low MSE and BIAS with small noise variance. However, as the noise variance increases the performance of Hasan A deteriorates in terms of MSE and BIAS.

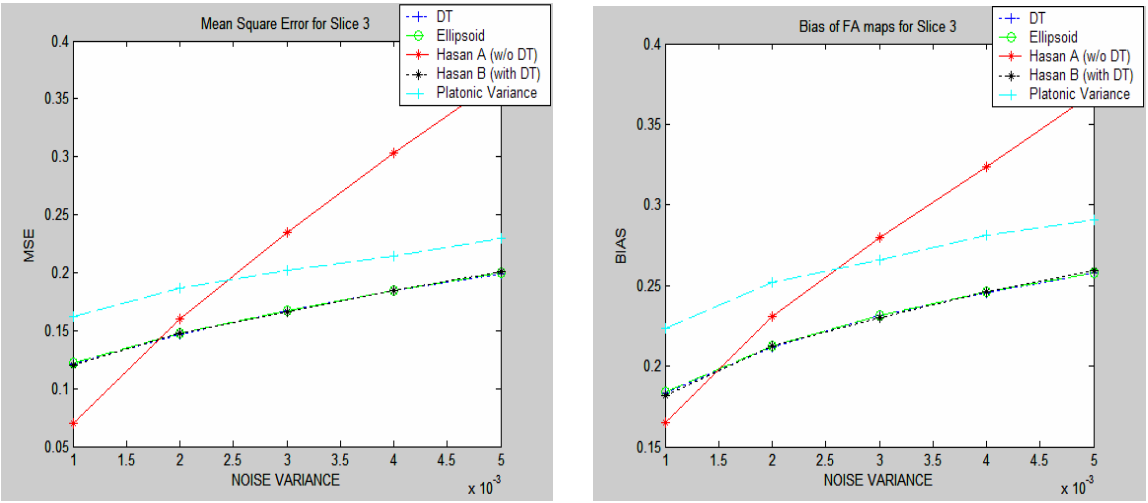

Figure 5.10 Plot of MSE and BIAS of FA v/s noise variance for slice 3

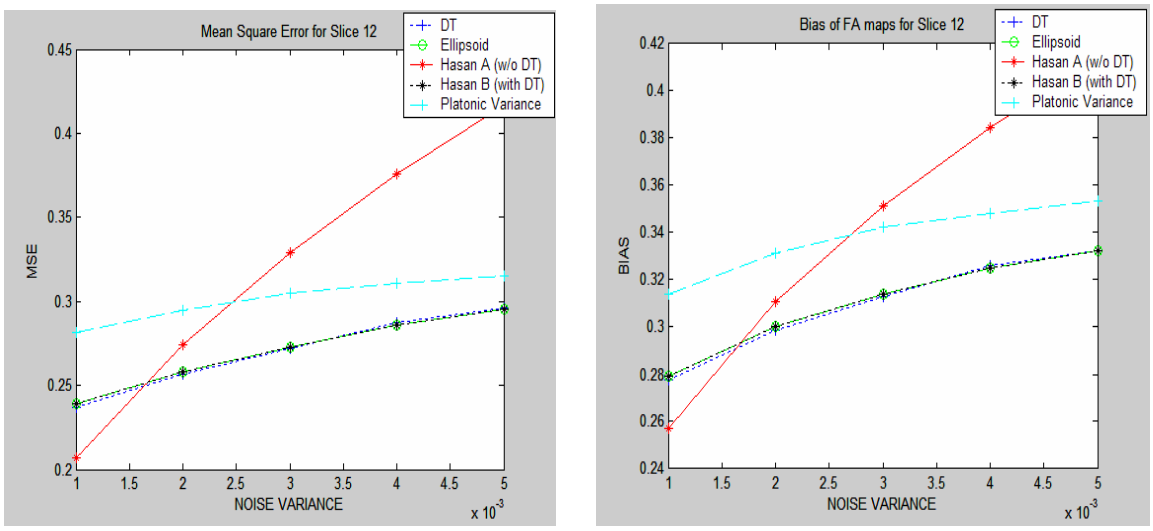

Figure 5.11 Plot of MSE and BIAS of FA v/s noise variance for slice 12

The results for only Slices 3 and 12 are shown for brevity; however we have generated results for the whole brain data set.

5.3 Comparison of Simulated and Human Brain MRI Data

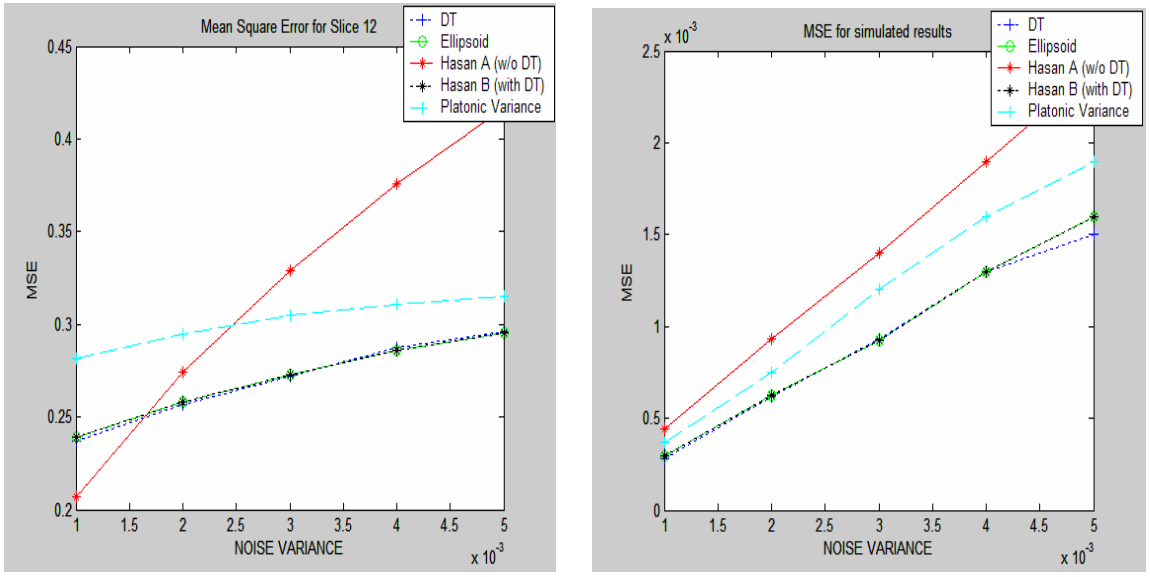

Figure 5.12: Plot of MSE of FA v/s noise variance for human MRI data and simulated data

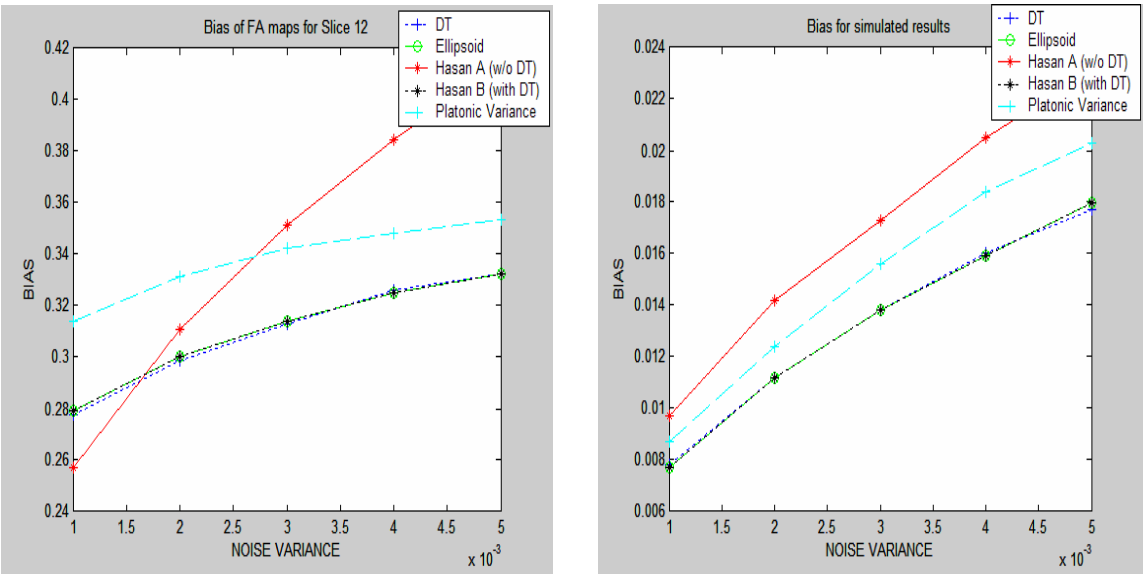

Figure 5.13 Plot of BIAS of FA v/s noise variance for human MRI data and simulated data

We observed similar results for MSE and BIAS of FA for the simulated and the human data (see Figure 5.12). Under a given noise variance, for the simulated and the human data, the DT, the Ellipsoid method and the Hasan B method (with DT) gave almost the same results (Figure 5.13). They were the most robust to noise. The Platonic Variance method was less robust to noise relative to these three methods. The Hasan A method (without diffusion tensor) showed maximum MSE and BIAS compared to all the other methods. For the Hasan A method, we can observe in human data that a small amount of added noise variance, gives good results, however as the variance increases this method crosses the plots of all other methods leading to increases noise sensitivity. Thus the Hasan A method was the least robust to noise.

5.4 Improvement and Filtering Results

5.4.1 Results Following Filtering

Using the threshold based filtering and median filtering technique, mentioned in section 4.3.1 we get the results as shown in Figure 5.14. We can clearly observe the filtering in the background whereas the central part of the image is untouched.

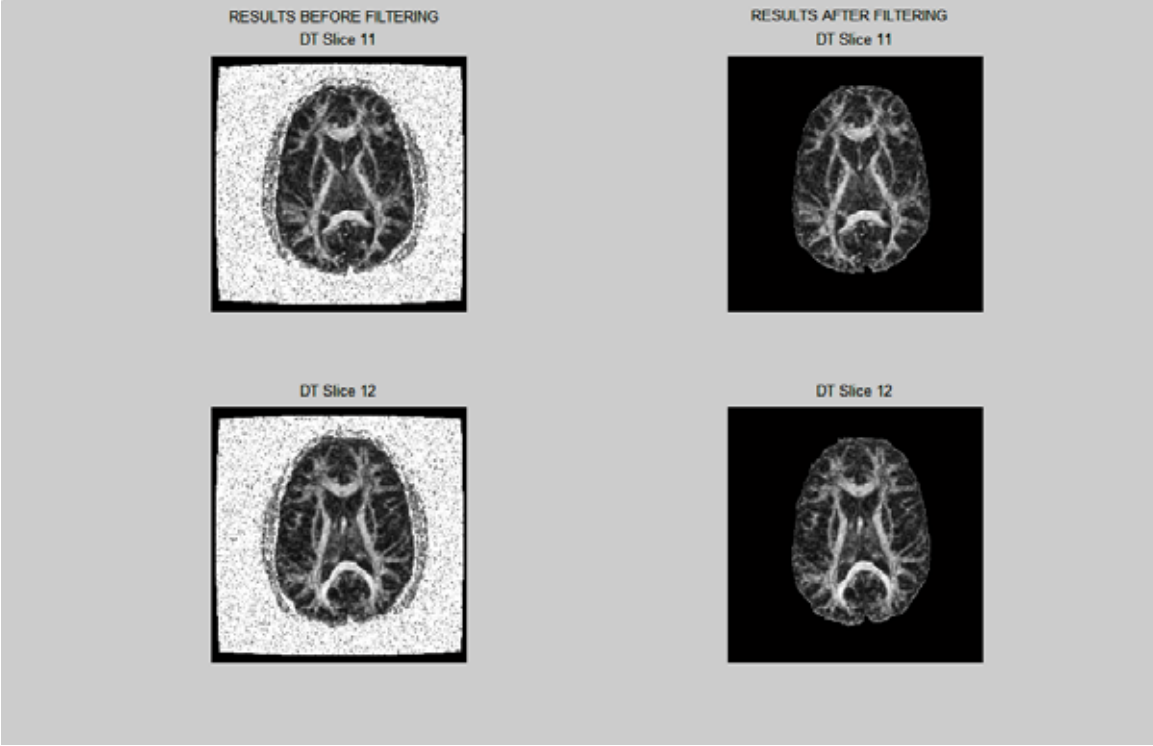

Figure 5.14 FA maps for slice 11 and 12 before (left) and after (right) filtering with NEX = 4

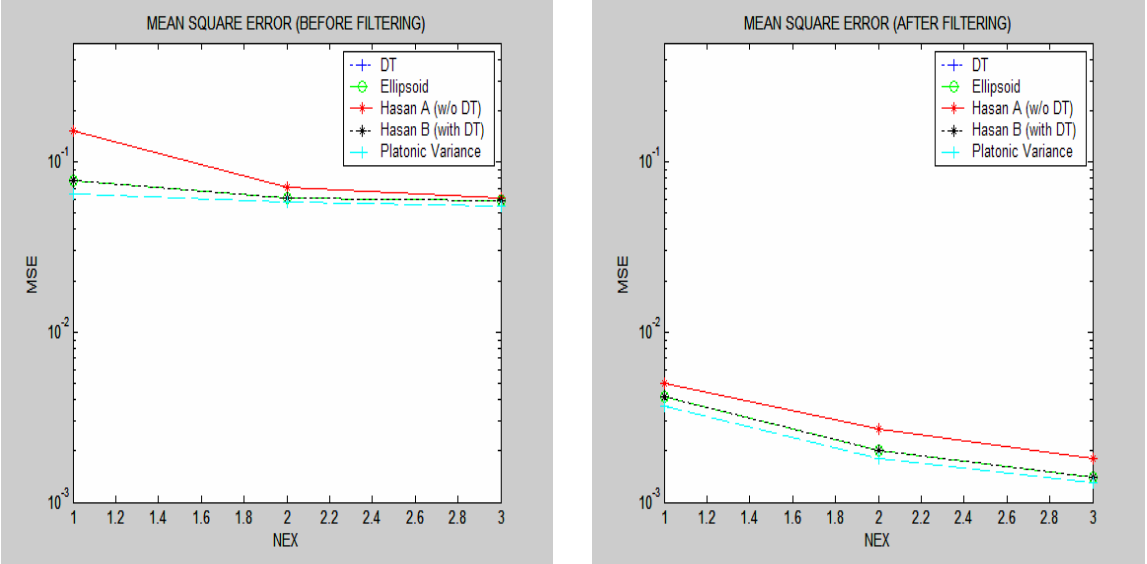

Figure 5.15 MSE for FA slice 12 before (left) and after (right) filtering

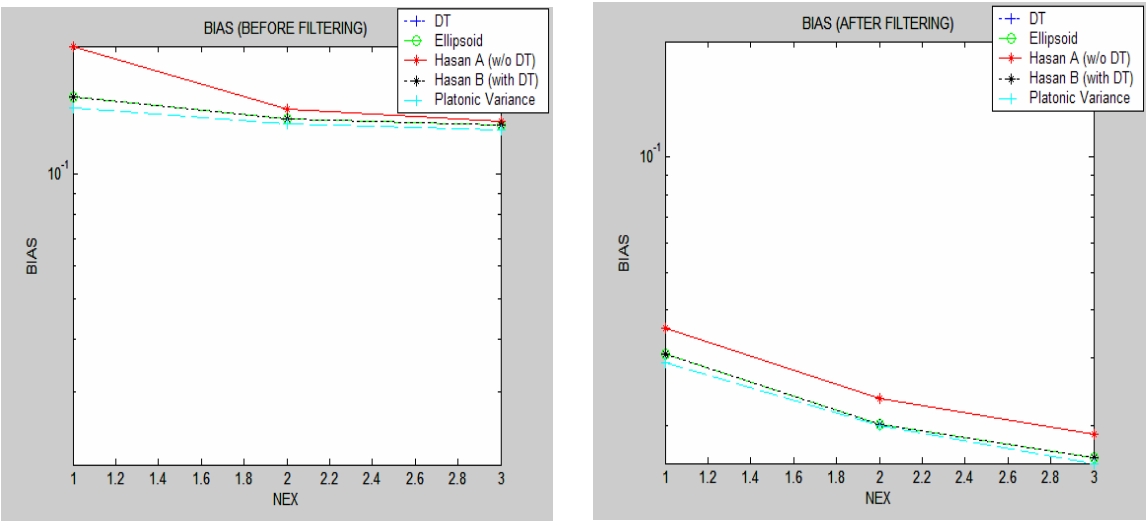

Figure 5.16 BIAS for FA slice 12 before (left) and after (right) filtering

Figure 5.15 and 5.16 shows plots for MSE and BIAS of FA for slice 12 before and after filtering. Using FA maps with $NEX = 4$ as the reference, MSE and BIAS are obtained for FA maps with $NEX = 1,2,3$. We can see a considerable reduction in the MSE and BIAS in Slice 12 before and after the filtering techniques. However it is still observed that Hasan A (without DT) shows maximum MSE and BIAS whereas the DT method, the Ellipsoid method and the Hasan B method (with DT) show similar results. The Platonic Variance method showed the minimum MSE and thus gives the best results.

Also the MSE and BIAS decrease as we increase the number of averages (acquisitions) from 1 to 3.

5.4.2 Results of Intervoxel Coherence Studies

Computing the average FA maps, difference with neighborhood pixels and a combination of averaging and difference with neighborhood pixels as mentioned in Section 4.4 yields the results as shown in Figure 5.17. The FA maps in these results are obtained using the DT method.

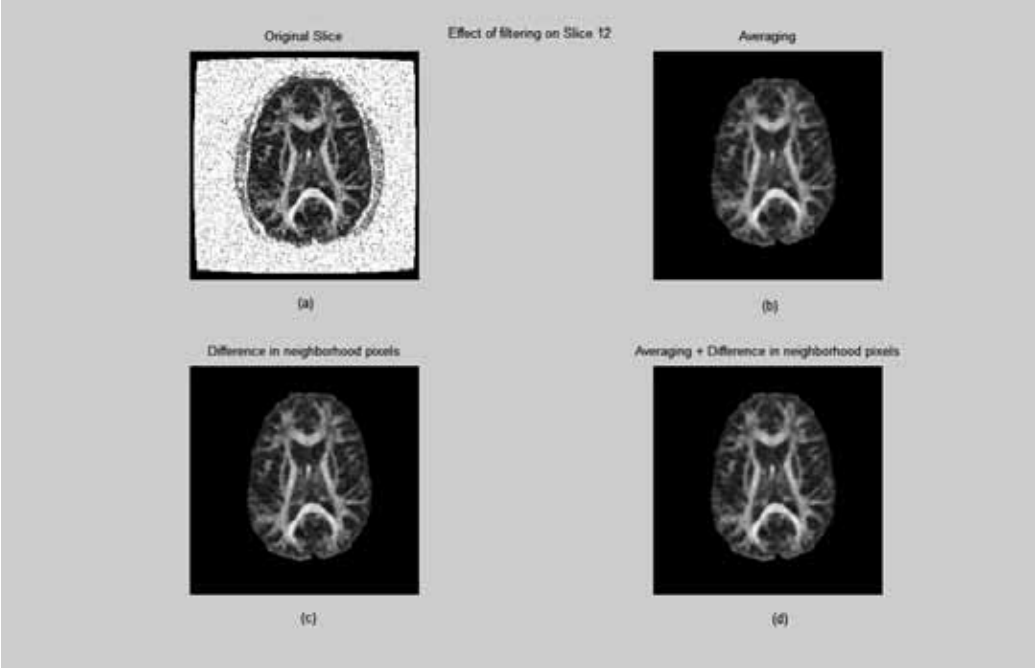

Figure 5.17 : Effects of intervoxel coherence on slice 12 with NEX = 4 using the DT method (a) Original slice 12 (b) Slice 12 after averaging method (c) Slice 12 after neighborhood difference method (d) Slice 12 after combining averaging and neighborhood difference

As observed we get homogeneous and smoother images on using the intervoxel coherence methods. We have obtained plots of MSE and BIAS of FA maps with intervoxel coherence for slice 12 as shown in Figures 5.18 and 5.19 respectively.

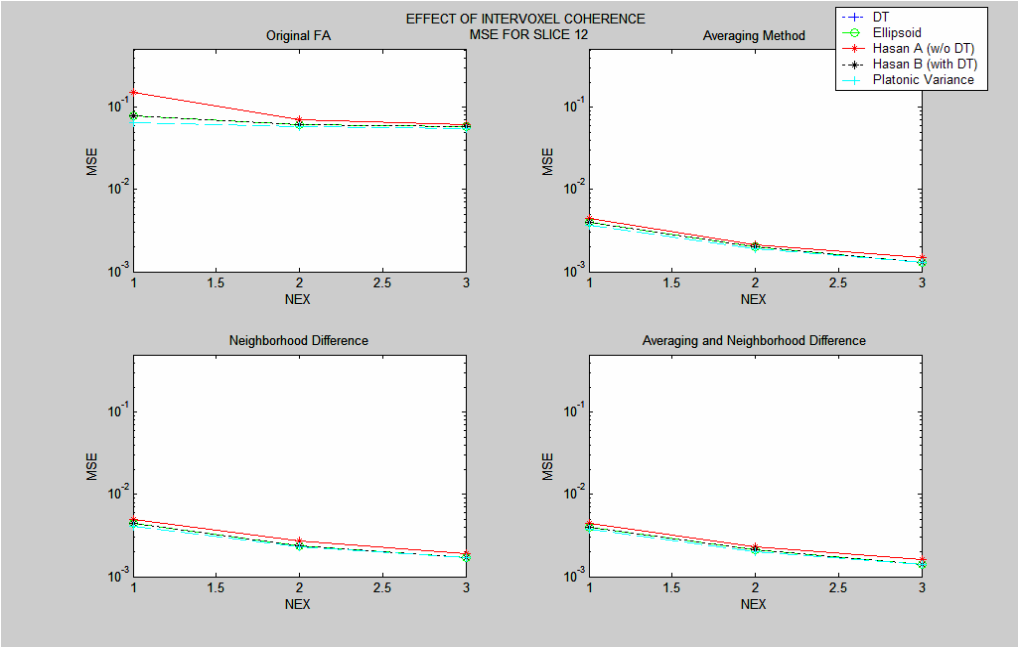

Figure 5.18 Effect of intervoxel coherence on MSE for FA slice 12

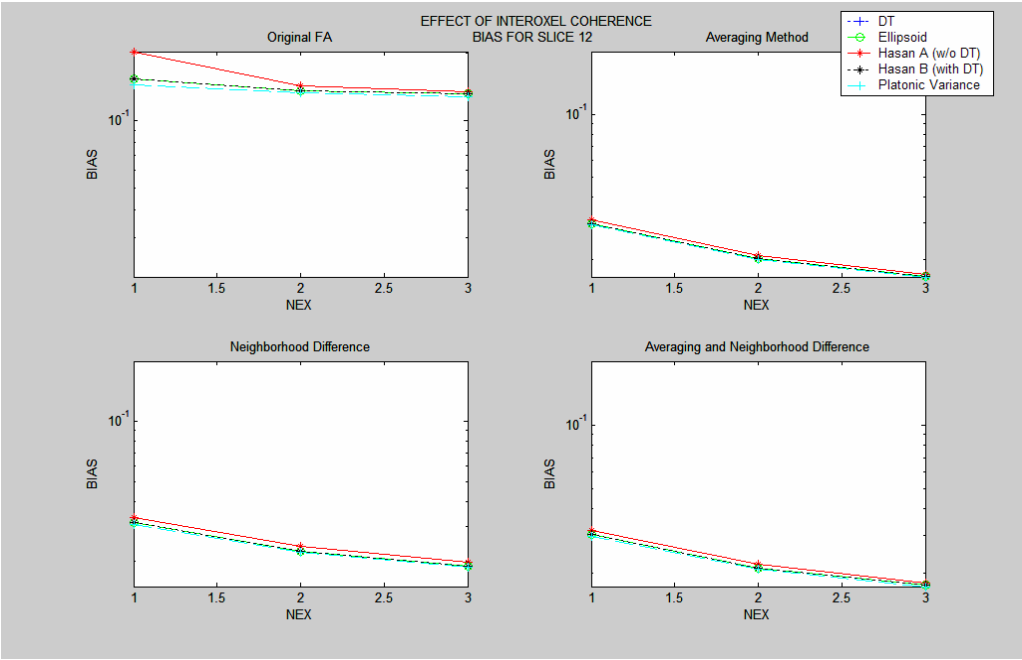

Figure 5.19 Effect of intervoxel coherence on BIAS for FA slice 12

5.5 Computational Cost

It would be the most advantageous to compute FA maps online; hence it is important to know the time efficiency of these methods. The amount of computation time for each of the method was calculated using both the simulated and human data. In the case of simulated data we obtained results by varying the number of directions as 6, 10, and 16. We used these specific directions, as the Platonic Variance method can only be used for these directions [5]. From the graph as shown in Figure 5.20 for the simulated data we observe that the Hasan B method (without DT) shows maximum computational efficiency followed by the Platonic Variance method. It can be seen that the computation time for each method increases with increase in the number of directions. For 20 and 26 directions we have not computed the computation time by the Platonic Variance method, as the Platonic Variance method does not support solids with 20 and 26 sides.

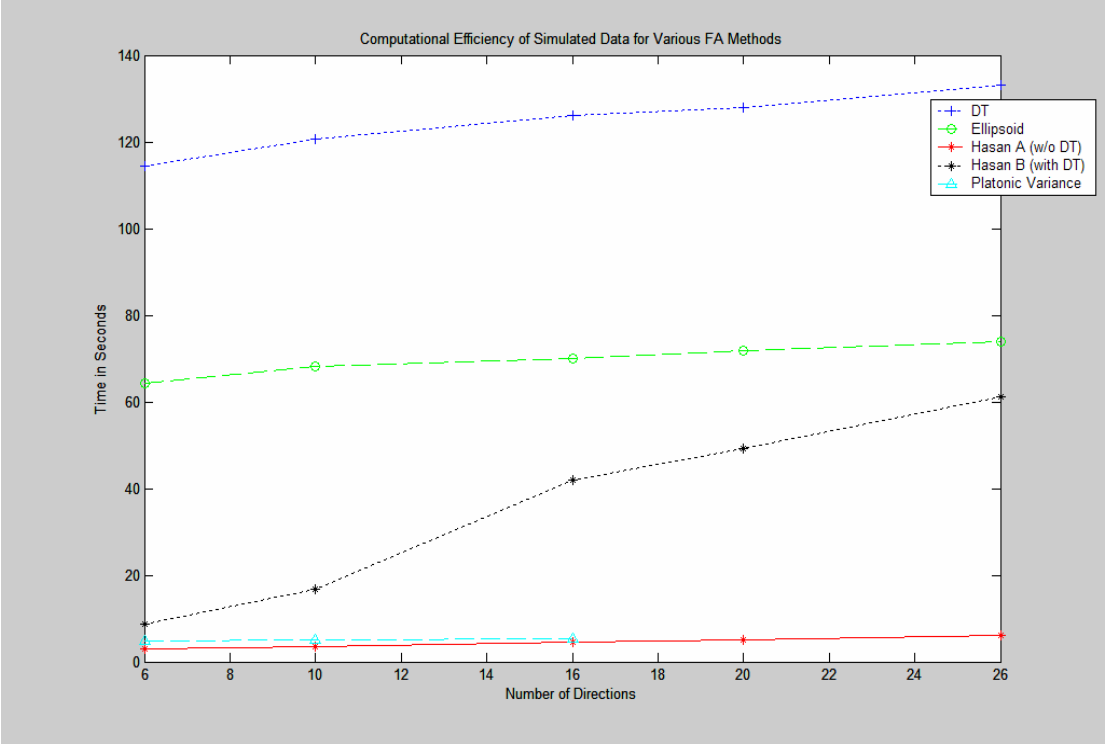

Figure 5.20 Time computation (in seconds) for different FA methods for simulated data with six slices and varying number of directions

Table 5.3 shows computation times, in seconds, for both the simulated and human brain MRI data. We could vary the number of directions for simulated data [only in a limited fashion though], but the human brain MRI data were acquired using 6 directions. However, we observed that for both types of data the Hasan B method (without DT) gave the best results in terms of time followed by the Platonic Variance method. From the computational performance, it can be observed that although Hasan B method is the least robust in the presence of noise, the method could indeed be useful for clinical applications that require immediate feedback.

Table 5.3 Computation time (seconds) for simulated and human brain MRI data

Simulated Data (128x128)					
Number of directions	**DT**	**Ellipsoid**	**Hasan A (w/o D)**	**Hasan B (with D)**	**Platonic**
6	114.328	64.328	**2.875**	8.796	4.875
10	120.593	68.234	**3.532**	16.719	5
16	125.984	70.015	**4.546**	41.922	5.266
20	127.813	71.7650	**5.1720**	42.3280	-
26	133.031	73.9840	**6.1250**	45.2190	-
Human Brain MRI Data (256x256)					
Number of directions	**DT**	**Ellipsoid**	**Hasan A (w/o D)**	**Hasan B (with D)**	**Platonic**
6	236.391	137.266	**4.5780**	22.641	9.078

5.6 Comparison of the Four FA Methods

Table 5.4: Comparison of the four FA methods

FA method	**Noise robustness 1 – Minimum, 3 – Maximum**	**Computationally efficient 1 – Minimum, 5 – Maximum**
Diffusion Tensor	2	1
Diffusion Ellipsoid	2	2
Hasan A (without DT)	1	5
Hasan B (with DT)	2	3
Platonic Variance	3	4

The Hasan A (without DT) is computationally fast, but has minimum noise robustness. The Platonic Variance method has good noise robustness and computational

efficiency, but is limited to platonic solids only. The Diffusion Tensor, Diffusion Ellipsoid and Hasan B (with DT) methods give similar results, although amongst the three we can state that the Hasan Method B is the best as it has the same noise robustness compared to the other two, but is more computationally efficient.

Chapter 6: Conclusions and Future Work

6.1 Conclusions

DT-MRI has become an increasingly important modality for aiding the understanding of the organization of normal brain structures and the evolution of neurological and psychiatric disorders. DTI is an *in vivo* visualization MRI technique that provides quantitative information about the integrity and orientation of white matter tracts in the human brain. Artifacts, produced by the interaction of the patients body or the body functions with the imaging process and noise from the scanner will degrade the quality of the diffusion weighted images which will in turn propagate the error to the invariant anisotropy measures. In this thesis we have mainly studied the noise and error propagation in these anisotropies, in particular, FA, was studied from maps calculated using four different methods. We have derived formulae to compute the variances in error propagation for other DTI parameters such as Volume Ratio, Trace, Anisotropy Index and Ultimate Anisotropy.

We have implemented four methods previously used for generating the FA maps. Visual inspection indicated close concordance amongst the four methods. The DT, Ellipsoid and Hasan (with DT) methods gave almost the same FA values. The flow of this thesis begins with the elimination of background noise from the source image, while leaving the central part of the image (brain) untouched. This method followed by median filtering considerably reduced the MSE and the bias of the FA maps. Another filtering technique of intervoxel coherence was implemented on the FA maps. In these methods, the result of the averaging technique is better than those obtained with neighborhood difference in terms of error as well as computational efficiency. A set of simulated data was generated and their FA maps were obtained, to draw similarities and to validate the results obtained from the simulated and human brain images. It is seen that addition of noise has similar effects on both the simulated data and human data for a given FA technique.

Comparing the different FA techniques, it can be concluded that the Hasan A (without DT) has the least noise robustness, whereas the Platonic Variance method is most robust to noise. With regard to computational efficiency, the Hasan A (without DT) was the most efficient, followed by the Platonic Variance approach. Thus we can state that Platonic Variance approach yielded better results in terms of both dealing with noise and being time efficient. This method is limited to only platonic solids. However, the main advantage of the Hasan A method is the shorter computation time i.e. one can potentially compute the FA maps online. This is important for the clinical applications where immediate feedback is needed. The Platonic Variance and Hasan B method do not involve computing the DT in generating the FA maps. Rather, they can be derived directly from the pixel values of the source images and are hence faster compared to the DT, Ellipsoid and Hasan B methods which generate FA maps from the DT thus leading to longer computation time. Overall, the Hasan B method is a good compromise with respect to time and noise robustness.

6.2 Future Work

In this thesis we studied the problem of noise and error propagation in DTI. We derived new relations for error propagation for various anisotropy indices. This work can be extended to implement the formulae for variances in error propagation in the different DTI parameters. Thereafter, depending on the results, instead of using FA as an invariant anisotropy measure, we can use other invariant DTI parameters that provide less variance in error propagation. This will improve the evaluation of the tract disruption in the brain. This can be also studied by addition of noise to all the different DTI parameters and computing its noise robustness and time efficiency, thus using the most efficient invariant measure for DTI. We can investigate the limits of noise robustness due to increasing number of averages and limiting the number of directions.

Bibliography

[1] R. Sigal, D. Doyon, Ph. Halimi, H.Atlan, "Magnetic resonance imaging basis for interpretation", *Springer Verlag*, December 1997

[2] L. Bihan, J.Mangin, C. Poupon, C. Clark, S. Pappata, N. Molko, H. Chabria, "Diffusion tensor imaging: concepts and applications", *J. Magn Reson Imaging* 2001; 13:534-546

[3] U. AM, V. Zijl PC, "Orientation independent diffusion imaging without tensor diagonalization: anisotropy definitions based on physical attributes of the diffusion ellipsoid", *J. Magn Reson Imaging* 1999; 9:804-813

[4] K. Hasan, P. A. Narayana, "Computation of fractional anisotropy and mean diffusivity maps without tensor decoding and diagonalization: Theoretical analysis and validation", *Magn Reson Med* 2003; 50:589-598

[5] E. Akkerman, "Efficient measurement and calculation of MR diffusion anisotropy images using the platonic variance method", *Magn Reson Med* 2003; 49:599-604

[6] Poonawala, X. Zhou, "Analytical error propagation in diffusion anisotropy calculations", *J. Magn Reson Imaging* 2004; 19:489-498

[7] P. Basser, C. Pierpaoli, "A simplified method to measure the diffusion tensor from seven MR images", *Magn Reson Med* 1998; 39:928-934

[8] H. Gudbjarston, S. Patz, "The rician distribution of noisy MRI data", *Magn Reson Med* 1995; 34:910-914

[9] J. Mattiello, P. Basser, D. Le Bihan, "Analytical expressions for the b matrix in NMR diffusion imaging and spectroscopy", *J. Magn Reson A* 1994; 108:131-141

[10] B. Wunsche, "Advanced texturing techniques for the effective visualization of neuroanatomy from diffusion tensor imaging data", *Conference in research and practice in information technology*, Vol. 29, 2004

[11] S. Pajevic, C. Pierpaoli, "Color Schemes to represent the orientation of anisotropic tissues from diffusion tensor data: applications to white matter fiber tract mapping in the human brain", *Magn Reson Med*, 1999; 42:526-540

[12] P. Basser, J. Mattiello, D. Le Bihan, “MR diffusion tensor spectroscopy and imaging”, *Biophys J* 1994; 66:259-267

[13] R. Bammer, M. Auer, S. Keeling, M. Augustin, L. Stables, R. Stollberger, M. Moseley, F. Fazekas, “Diffusion tensor imaging using single shot sense SENSE-EPI”, *Magn Reson Med*, 2002; 48:128-136

[14] C. Pierpaoli, P. Jezzard, P. Basser, A. Barnett, G. Chiro, “Diffusion tensor MR imaging of the human brain”, *Radiology*, 1993; 201:637-648

[15] N. Papadakis, D. Xing, G. Houston, J. Smith, M. Smith, M. James, A. Parsons, C. Huano, L. Hall, A. Carpenter, “Study of rotationally invariant and symmetric indices on diffusion anisotropy”, *Magn Reson Imaging* 1999; 17:881-892

[16] S. Skare, M. Hedehus, M. Moseley, T. Li, “Condition number as a measure of noise performance of diffusion tensor data acquisition schemes with MRI”, *J. Magn Reson* 2000; 147:340-352

[17] D. Jones, M. Horsfield, A. Simmons, “Optimal strategies for measuring diffusion in anisotropic systems by magnetic resonance imaging”, *Magn Reson Med* 1999; 42:515-525

[18] P. Basser, J. Mattiello, D. Le Bihan, “Estimation of effective self-diffusion tensor from the NMR spin echo”, *J. Magn Reson B* 1994; 103:247-254

[19] P. Basser, “Diffusion tensor MRI: theory experimental design and data analysis”, *NMR Biomed 2002; 15:456-467*

[20] S. Skare, T. Li, B. Nordell, M. Ingvar, “Noise considerations in the determination of diffusion tensor anisotropy”, *Magn Reson Imaging* 2000; 18:659-669

[21] E. Melhem, R. Itoh, L. Jones, P. Barker, “Diffusion tensor MR imaging of the brain: effect of diffusion weighting on trace and anisotropy measurements”, *AJNR* 2000; 21:1813-1820

[22] A. Anderson, “Theoretical analysis of the effects of noise on diffusion tensor imaging”, *Magn Reson Med* 2001; 46:1174-1188

[23] P. E. Sullivan, M. Hedehus, K. Lim, E. Adalsteinsson, M. Moseley, “Age related decline in brain white matter anisotropy measured with spatially corrected echo-planar diffusion tensor imaging”, *Magn Reson Med* 2000; 44:259-268

[24] C. Pierpaoli, P. Basser, “Toward a quantitative assessments of diffusion anisotropy”, *Magn Reson Med* 1996; 36: 893-906

[25] K. M. Smith, “Magnetic resonance imaging: principles and applications”, *William Heinemann Medical Books*, 1986

[26] R. Sigal, “Magnetic resonance imaging: basis for interpretation”, *Springer Velag*, 1998

[27] R. Smith, R. Lange, “Understanding magnetic resonance imaging”, *CRC*, 1989

[28] URL: http://www.psych.stanford.edu/~kalina/BB (date retrieved: March 2005)

[29] A. Taylor, “Diffusion tensor imaging: evaluation of tractography algorithm performance using ground truth phantoms, 2004, Blacksburg, VA

[30] URL: http://www.med.nagasaki-u.ac.jp/radiology (date retrieved: March 2005)

[31] URL: http://www.diagnosticimaging.com/advancedMR/diffusion.jhtml (date retrieved: March 2005)

[32] URL: http://www.alumni.ca/~tsej4j0/background2.html (date retrieved: March 2005)

[33] URL: http://www.mr-tip.com (date retrieved: March 2005)

[34] URL: http://www.med.nagasaki-u.ac.jp/radiology (date retrieved: March 2005)

[35] P. Sprawls, Magnetic resonance imaging: principles, methods and techniques, *Medical Physics Publishing*, 2000

[36] URL: http://www.sghms.ac.uk/depts/cn/research/dti.html (date retrieved: March 2005)

[37] URL: http://www.enchantedlearning.com/subjects/anatomy/brain/glossary/ (date retrieved: March 2005)

[38] M. Kubicki, C. Westin, S. Maier, H. Mamata, M. Frumin, H. Hershfield, R. Kikinis, F. Jolesz, R. McCarley, M. Shenton, “Diffusion tensor imaging and its applications to neuropyschiatric disorders” , *President and Fellows of Harvard College*, 2002

[39] S. Pinker, “The best American science nature and writing”, *Houghton Mifflin*, 2004

[40] P. Basser, C. Pierpaoli, “Microstructural and physiological features of tissues elucidated by quantitative diffusion tensor MRI”, *J. Magn Reson B* 1996, 111:209-219

Appendix

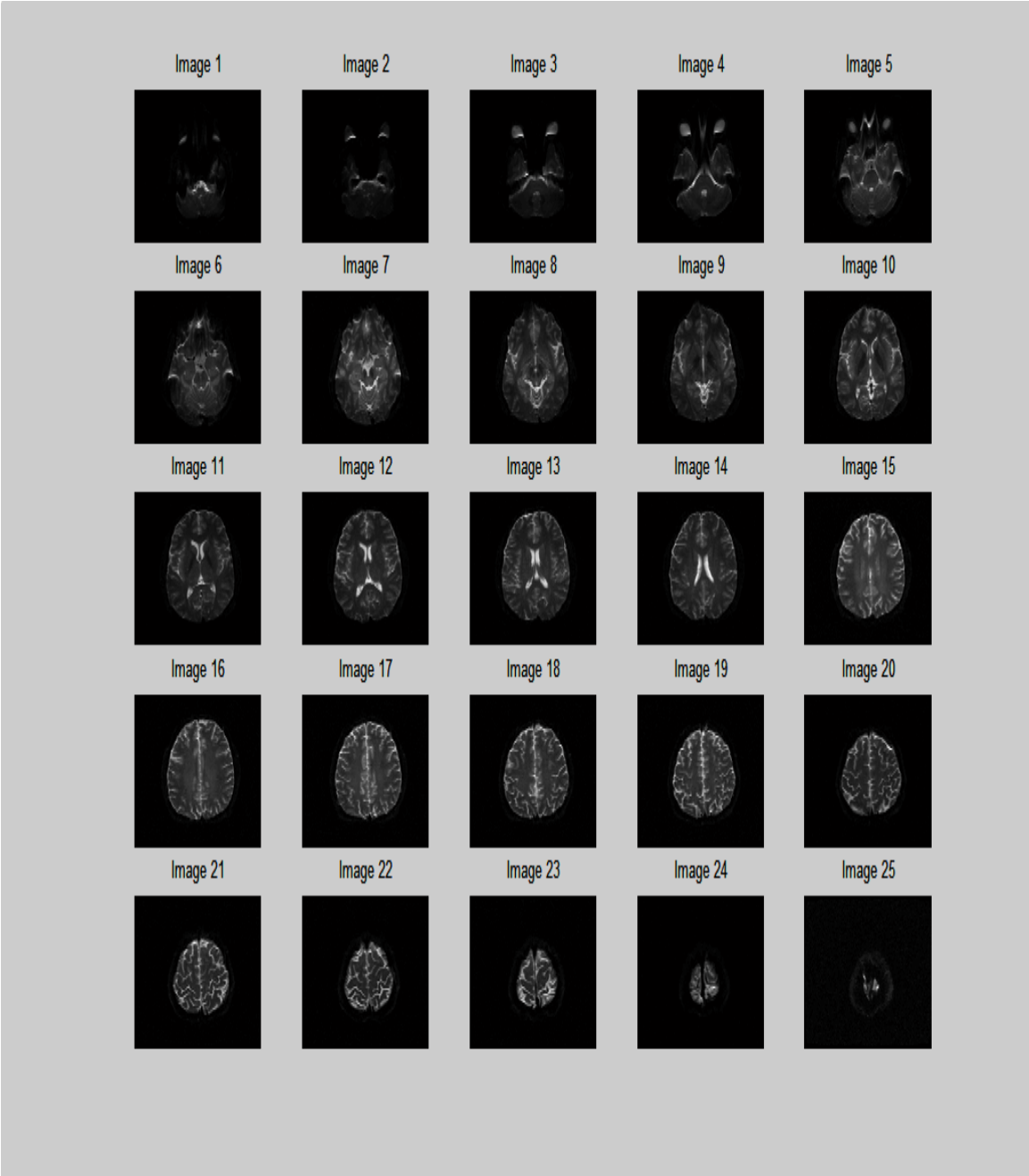

Figure A1: Slices 1-25 of human brain MRI data with NEX = 4

Directions 1-6 refer to the six different directions in which the human brain MRI data was acquired.

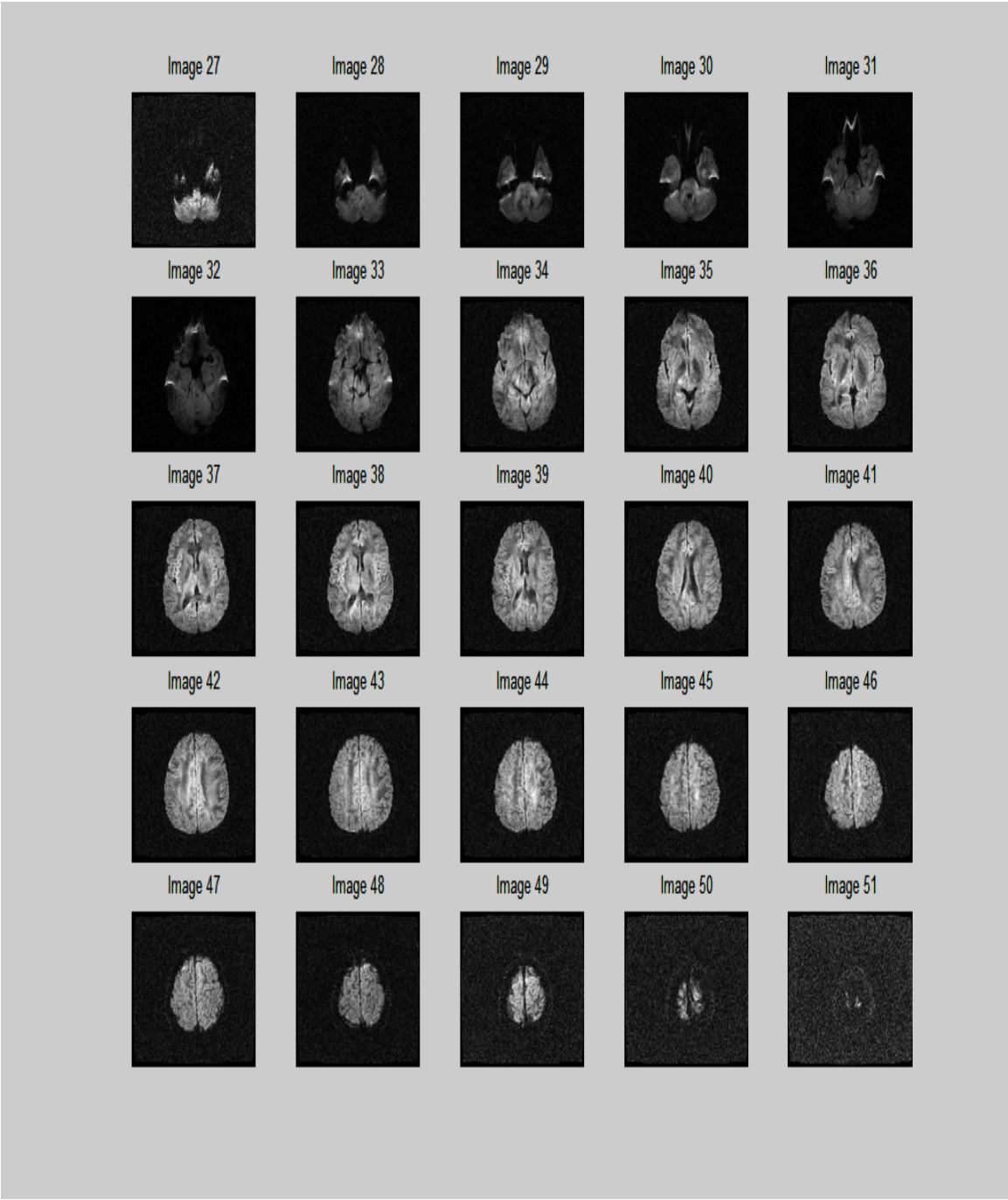

Figure A2: Slices 1-25 in direction 1 of human brain MRI data with NEX = 4

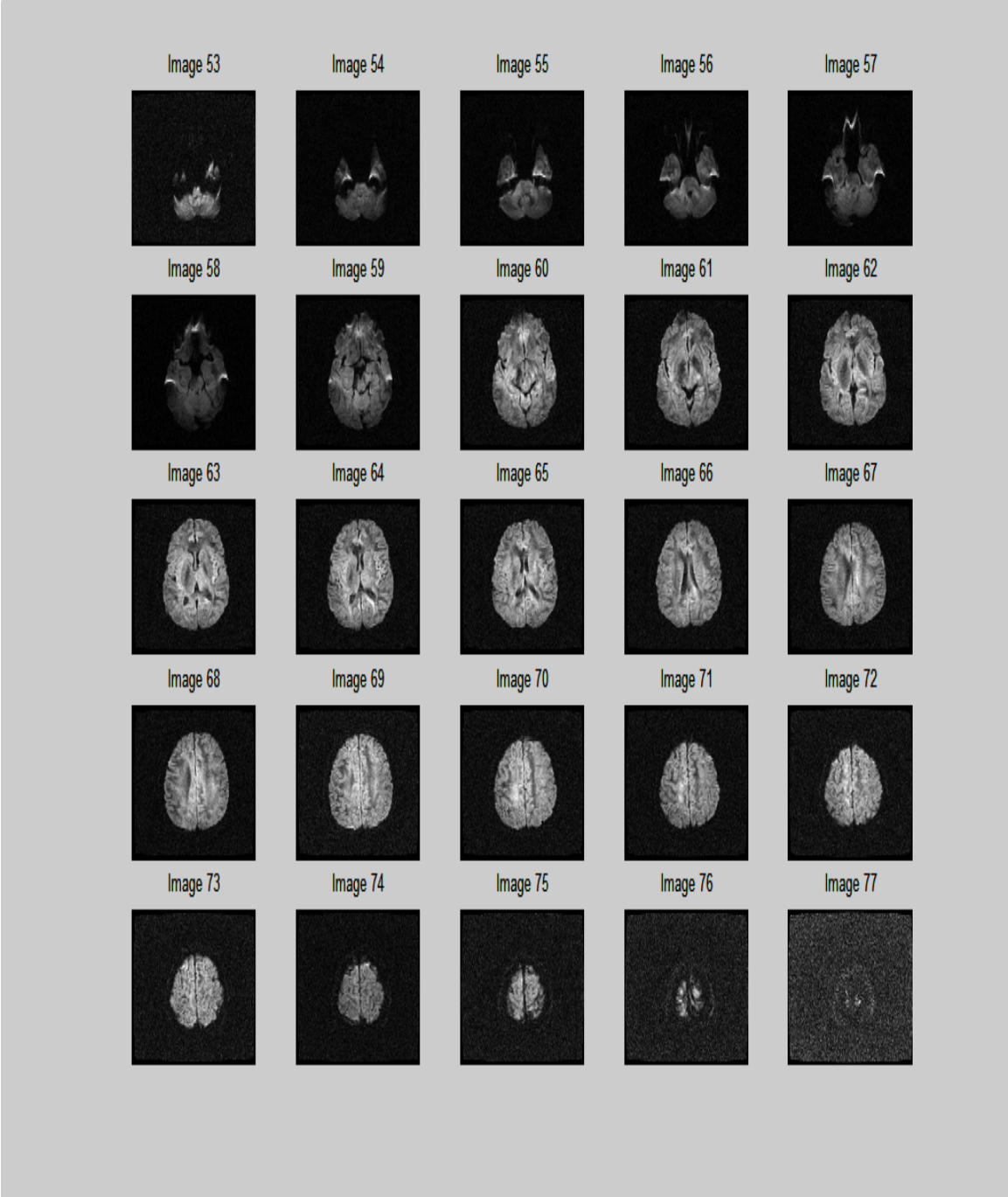

Figure A3: Slices 1-25 in direction 2 of human brain MRI data with *NEX = 4*

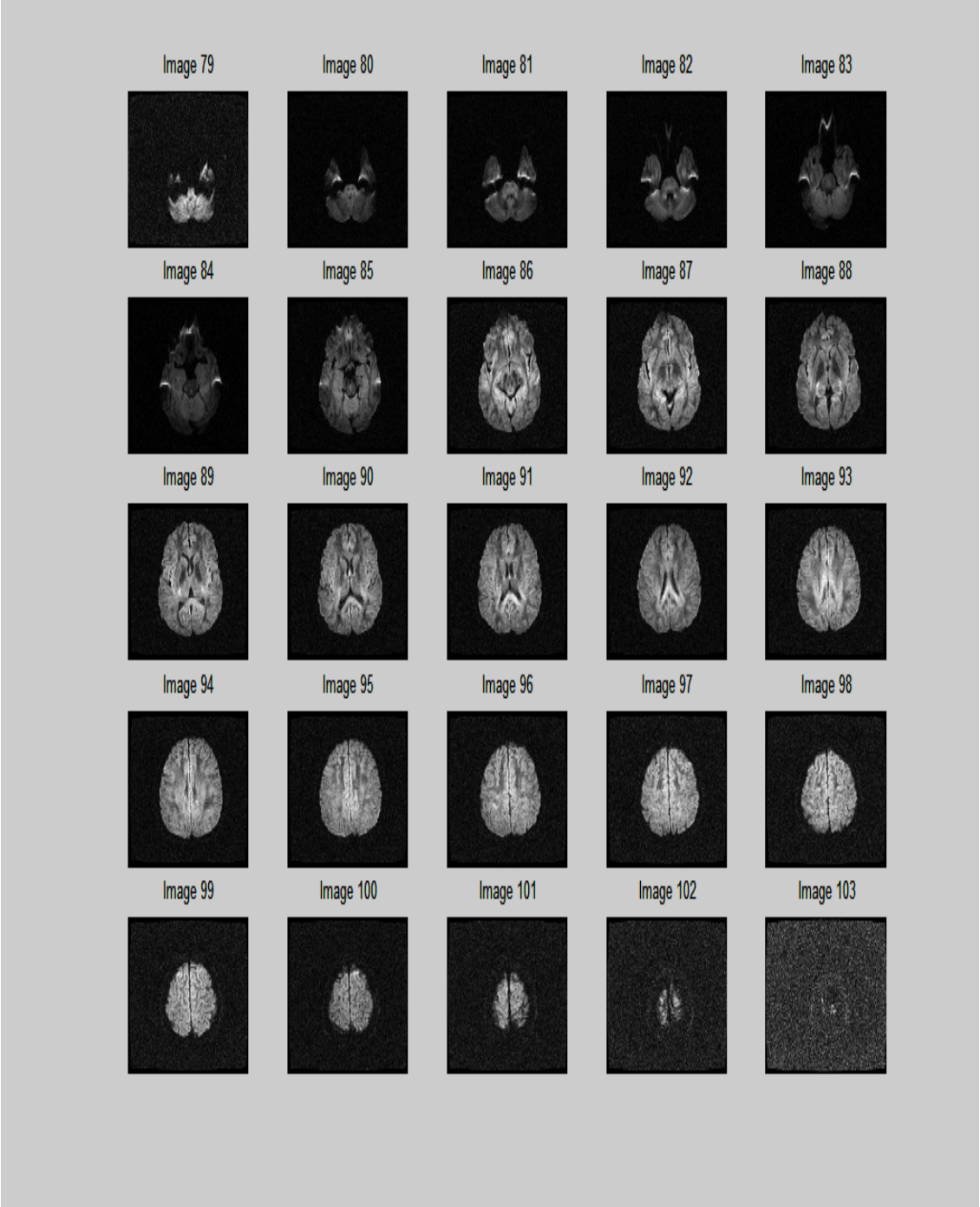

Figure A4: Slices 1-25 in direction 3 of human brain MRI data with NEX = 4

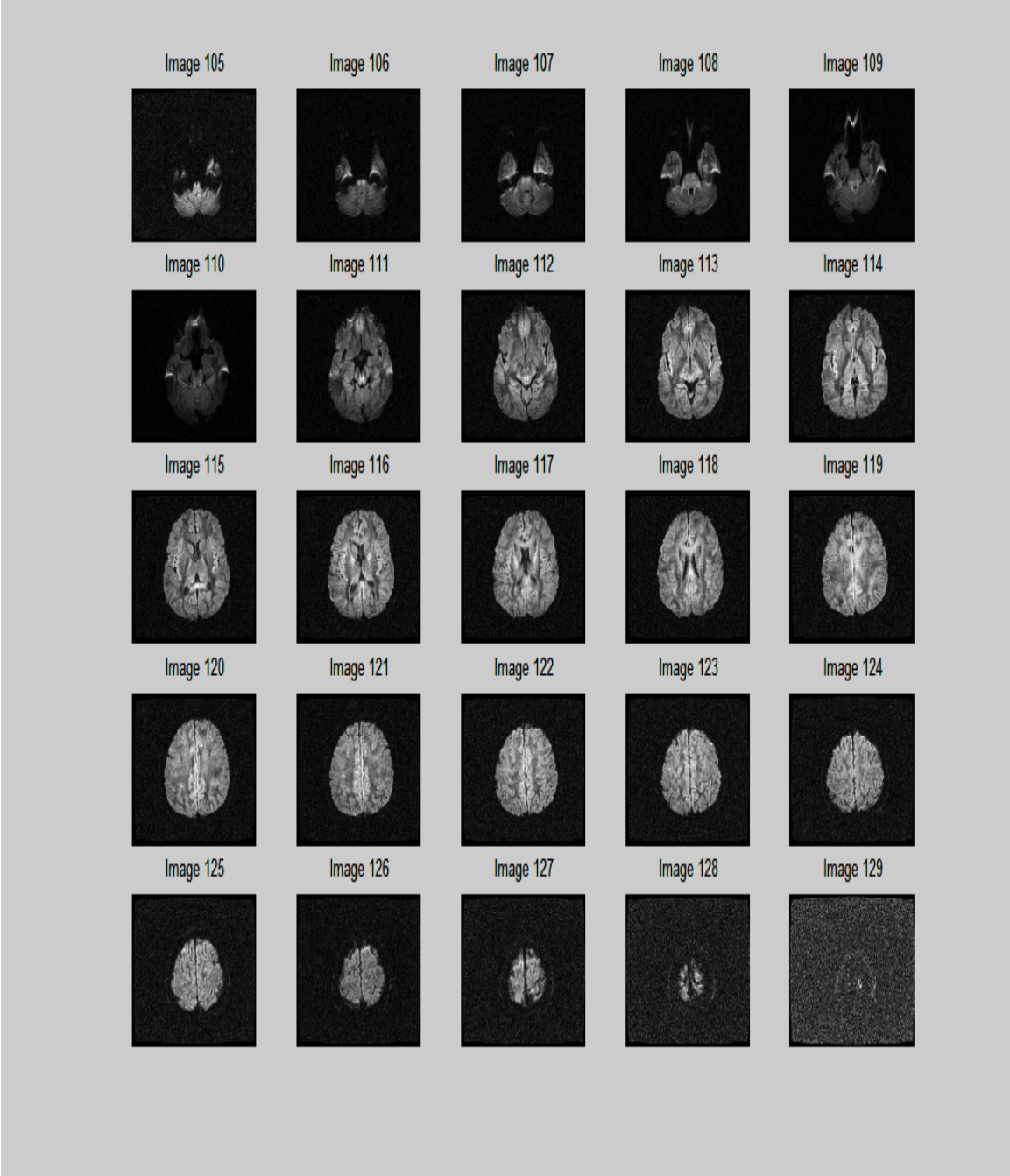

Figure A5: Slices 1-25 in direction 4 of human brain MRI data with NEX = 4

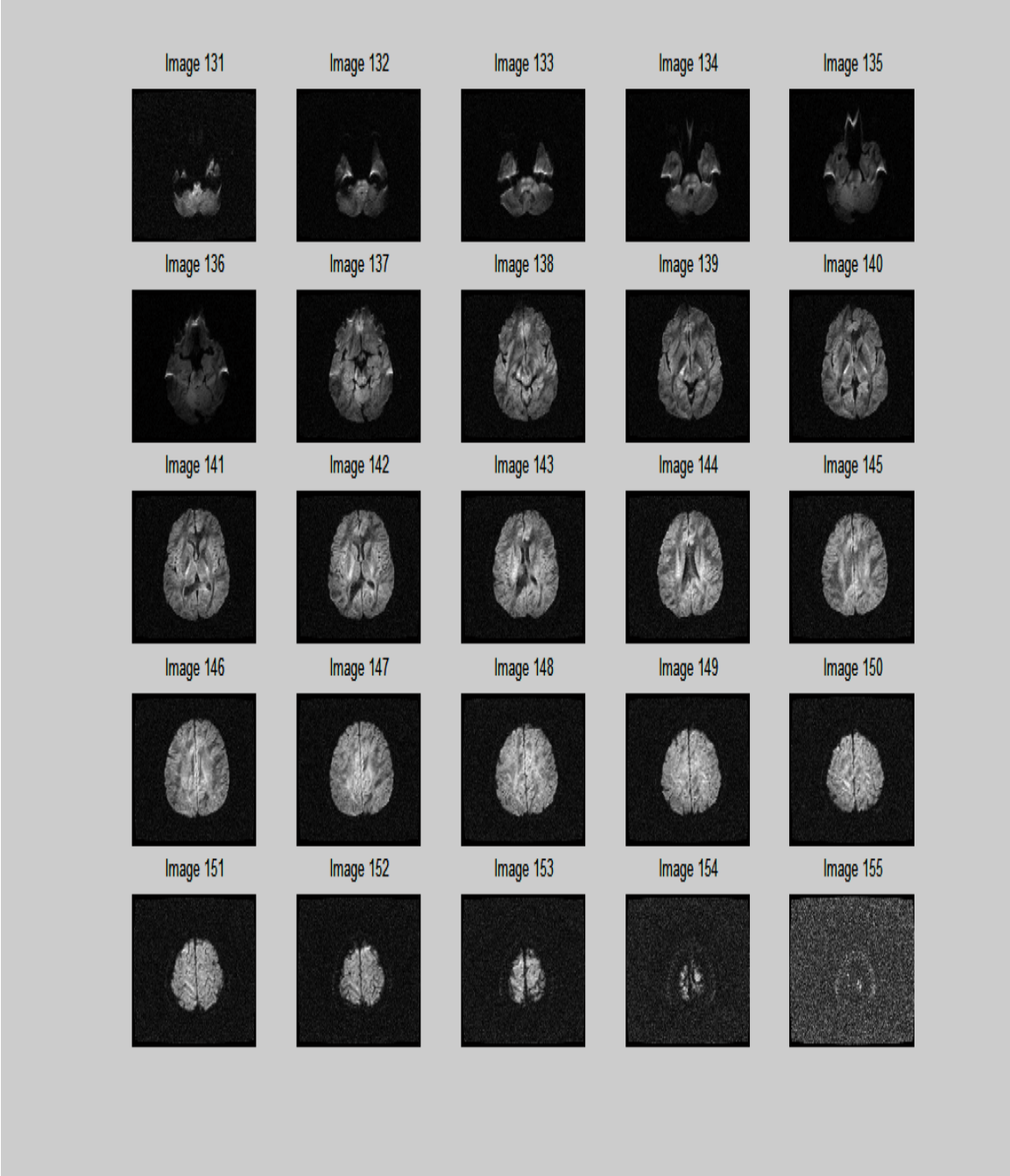

Figure A6: Slices 1-25 in direction 5 of human brain MRI data with NEX = 4

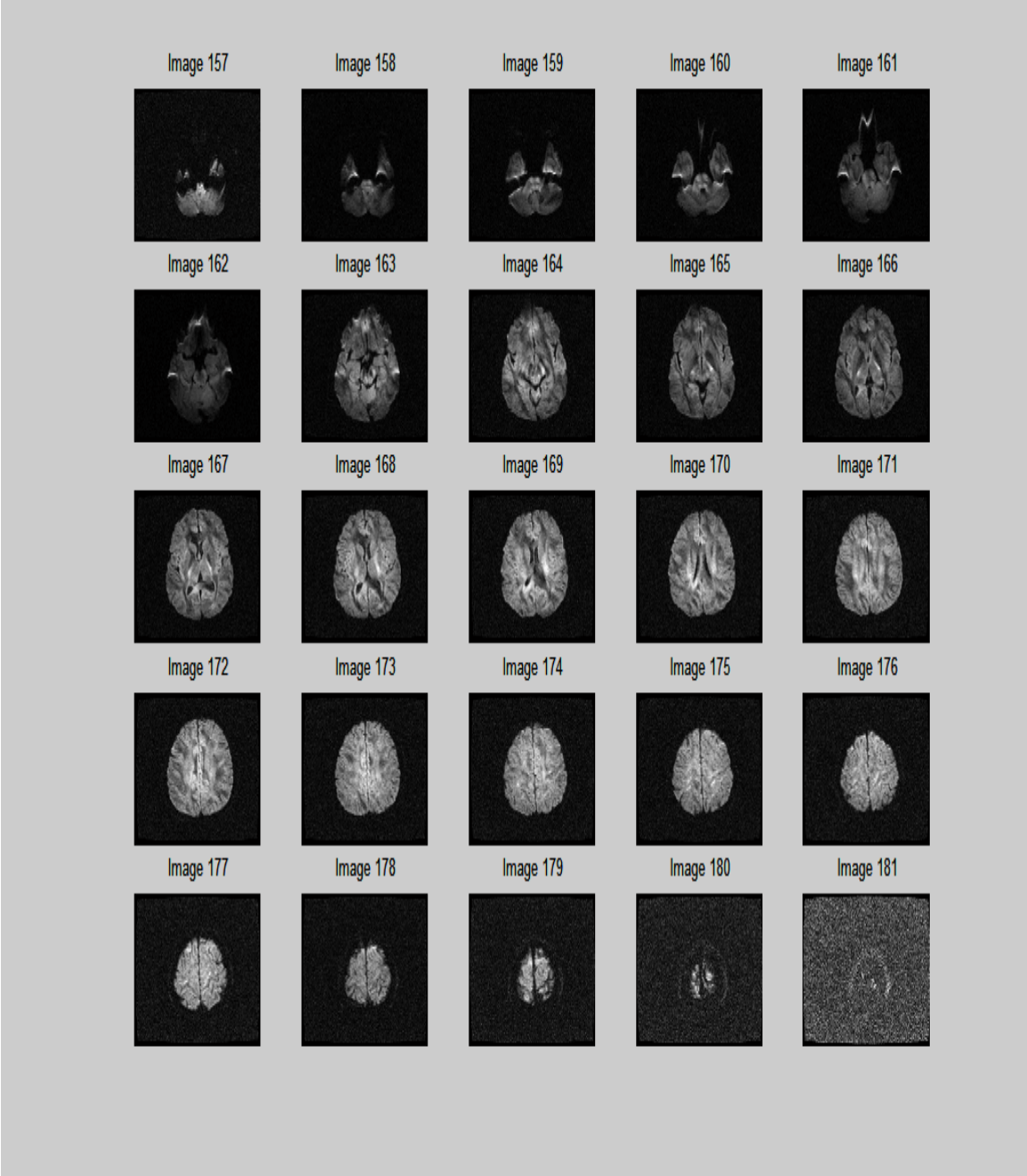

Figure A7: Slices 1-25 in direction 6 of human brain MRI data with NEX = 4

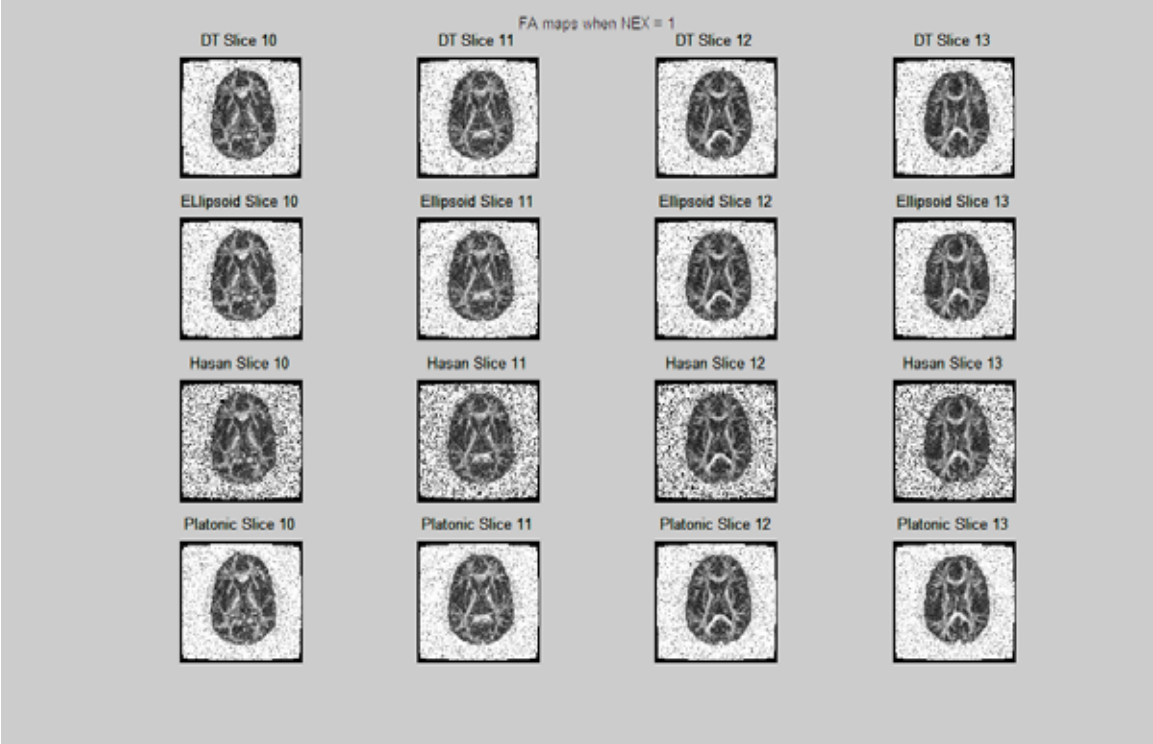

Figure A8: FA maps using the four methods with NEX = 1

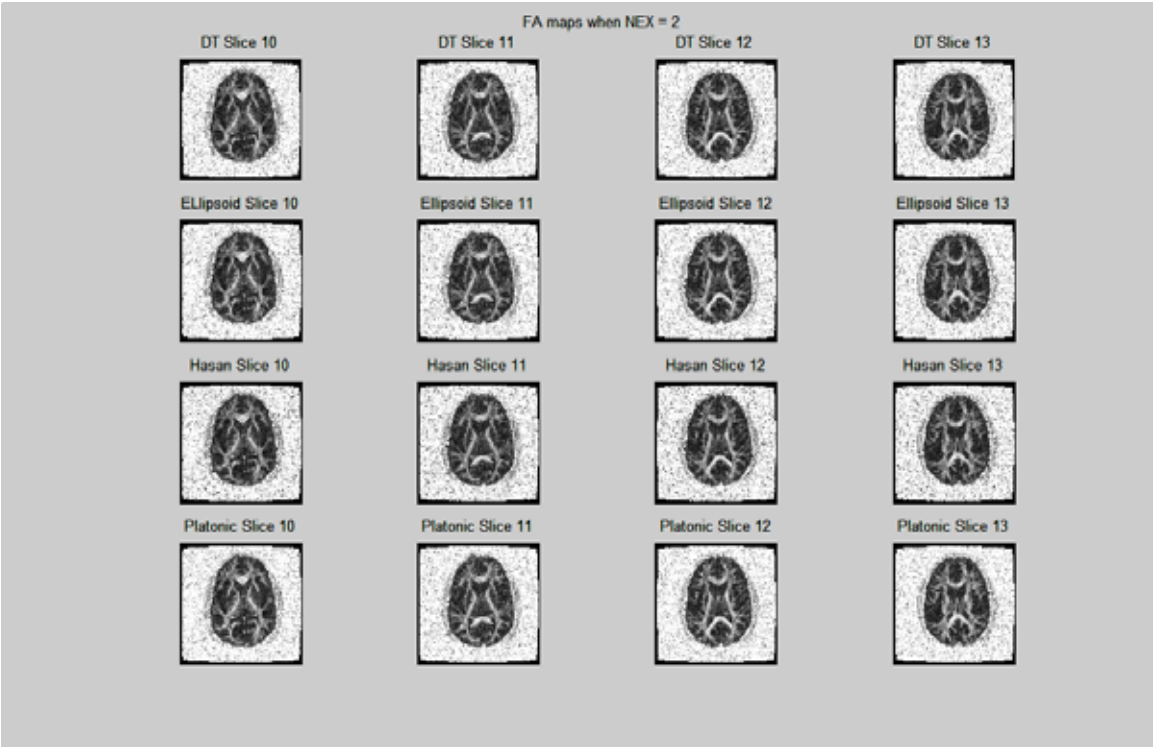

Figure A9: FA maps using the four methods with NEX = 2

Figure A10: FA maps using the four methods with NEX = 3